



## Article

**Cite this article:** Scambos TA *et al.* (2025) AMIGOS-3 multi-sensor stations and the climate, ice and ocean conditions at Thwaites Eastern Ice Shelf during 2020–22. *Journal of Glaciology* **71**, e60, 1–0. <https://doi.org/10.1017/jog.2024.96>

Received: 11 April 2024

Revised: 18 October 2024

Accepted: 5 November 2024

**Keywords:**

automation; climate change; field observations; glaciology; instrumentation

**Corresponding author:** Ted A. Scambos;

Email: [tascambos@colorado.edu](mailto:tascambos@colorado.edu)

Now at:

<sup>a</sup>Workday, Boulder, CO, USA.

<sup>b</sup>Department for Geoscience, University of Tübingen, Tübingen, Germany.

<sup>c</sup>Arora Consulting Services LLC, Denver, CO, USA.

<sup>d</sup>Aerospace Engineering and Biomedical Engineering, University of Colorado Boulder, Boulder CO, USA.

<sup>e</sup>Airbus U.S. Space and Defense, Denver, CO, USA.

<sup>f</sup>Nidec Institutional Solutions, Northfield, OH, USA.






<sup>g</sup>Boeing Defense, St. Louis, MO, USA.

<sup>h</sup>L3Harris Technologies, Colorado Springs, CO, USA.

<sup>i</sup>Sierra Space, Boulder, CO, USA.

<sup>j</sup>National Oceanography Centre, Southampton, UK.

# AMIGOS-3 multi-sensor stations and the climate, ice and ocean conditions at Thwaites Eastern Ice Shelf during 2020–22

Ted A. Scambos<sup>1</sup> , T. White<sup>2</sup>, B. Wallin<sup>3,a</sup>, M. Truffer<sup>4</sup> , G. Collao-Barrios<sup>5</sup>, C. Kratt<sup>6</sup>, S. Tyler<sup>6</sup>, E.C. Pettit<sup>7</sup> , C.T. Wild<sup>7,b</sup>, S. Arora<sup>8,c</sup>, S. Edwards<sup>8,d</sup>, R. Fotherby<sup>8,e</sup>, C. Meha<sup>8,f</sup>, J. Soltys<sup>8,g</sup>, E. Tomlinson<sup>8,h</sup>, R. Weatherby<sup>8,i</sup>, R. Ross<sup>9</sup>, A. Wählin<sup>10</sup>, T.S. Dotto<sup>11,j</sup>, K. Alley<sup>12</sup>  and A. Muto<sup>13</sup> 

<sup>1</sup>Earth Science Observation Center, CIRES, University of Colorado Boulder, Boulder, CO, USA; <sup>2</sup>Tim White Engineering, Broomfield, CO, USA; <sup>3</sup>National Snow and Ice Data Center, CIRES, University of Colorado Boulder, Boulder, CO, USA; <sup>4</sup>Geophysical Institute, University of Alaska Fairbanks, Fairbanks, AK, USA; <sup>5</sup>Institut des Geosciences de l'Environnement, Université Grenoble Alpes, Grenoble, France; <sup>6</sup>Department of Geological Sciences and Engineering, University of Nevada, Reno, NV, USA; <sup>7</sup>College of Earth, Ocean and Atmospheric Sciences, Oregon State University, Corvallis, OR, USA; <sup>8</sup>Space Grant, Engineering Department, University of Colorado Boulder, Boulder, CO, USA; <sup>9</sup>Polar66 Engineering, Sydney, Australia; <sup>10</sup>Department of Marine Sciences, University of Gothenburg, Göteborg, Sweden; <sup>11</sup>School of Environmental Sciences, University of East Anglia, Norwich, UK; <sup>12</sup>Centre for Earth Observation Science, Environment and Geography, University of Manitoba, Winnipeg, MB, Canada and <sup>13</sup>Department of Earth and Environmental Sciences, Temple University, Philadelphia, PA, USA

**Abstract**

The Automated Meteorology—Ice—Geophysics Observation System 3 (AMIGOS-3) is a multi-sensor on-ice ocean mooring and weather, camera and precision GPS measurement station, controlled by a Python script. The station is designed to be deployed on floating ice in the polar regions and operate unattended for up to several years. Ocean mooring sensors (SeaBird MicroCAT and Nortek Aquadopp) record conductivity, temperature and depth (reported at 10 min intervals), and current velocity (hourly intervals). A Silixa XT fiber-optic distributed temperature sensing system provides a temperature profile time-series through the ice and ocean column with a cadence of 6 d<sup>-1</sup> to 1 week<sup>-1</sup> depending on available station power. A subset of the station data is telemetered by Iridium modem. Two-way communication, using both single-burst data and file transfer protocols, facilitates station data collection changes and power management. Power is supplied by solar panels and a sealed lead-acid battery system. Two AMIGOS-3 systems were installed on the Thwaites Eastern Ice Shelf in January 2020, providing data well into 2022. We discuss the components of the system and present several of the data sets, summarizing observed climate, ice and ocean conditions.

**1. Introduction**

Year-round monitoring of environmental or geophysical systems is a key part of understanding the processes governing their evolution and identifying the events that characterize a response to change (e.g. climate change), leading to improvements in forecasting how the system will evolve. Establishing long-term automated monitoring is particularly difficult for polar locations because of the challenges imposed by the polar winter environment. Although a wide variety of autonomous observational systems for polar work have been developed since an earlier publication on similar stations (Scambos and others, 2013), most automated systems to date are aimed at a specific primary measurement (e.g. seismicity, ice or rock movement,



weather monitoring or ocean state). Here we describe a system designed to observe several environmental and geophysical parameters simultaneously, in regions where complex and interconnected changes are occurring. The areas of rapid ice-surface or basal melting, unusual ice-shelf or glacier dynamics or free-drifting icebergs are all potential sites for this kind of multi-sensor, multi-year observation system. Climate–ice–ocean observations, collected continuously for several years, greatly facilitate the understanding and modeling of local-scale interactions between climate (or weather), ocean circulation, ice loss and glacier acceleration. Automated Meteorology–Ice–Geophysics–Observation System-3 (hereafter, ‘AMIGOS-3’) stations have already contributed to several published studies spanning climate, ocean and glaciological processes on ice shelves (Lee and others, 2019; Alley and others, 2021; Wählin and others, 2021; Dotto and others, 2022, 2022; MacLennan and others, 2023).

Recent ice–ocean monitoring systems (sometimes called on-ice moorings) have mainly been developed for measurements of sea ice and the underlying near-surface ocean layer, and have generally been installed on Arctic sea ice in regions of high sea-ice concentration on thick, large, stable floes (e.g. Krishfield and others, 2008). Autonomous systems have been developed for measuring sea-ice mass balance, wave action within the pack, and upper ocean conditions, summarized in a paper discussing their application for the Marginal Ice Zone and Sea State program (Lee and others, 2017). Several sea-ice mass-balance stations were developed by the Office of Naval Research, the US Army Cold Regions Research and Engineering Laboratory and the British Antarctic Survey (Shaw and others, 2008; Polashenski and others, 2011; Doble and others, 2017). Automated ice–ocean systems on ice shelves have a less wide-ranging history and relatively few types of installations (e.g., Hatterman and others, 2012). A broadly similar station to the AMIGOS-3 was deployed on the Petermann Glacier floating ice tongue (briefly described in Münchow and others, 2016; Washam and others, 2019) consisting of several conductivities, temperatures and depths (CTDs), a GPS and a weather station installed through a borehole, with access to some data and sensor control through an Iridium link. Several systems deployed on the Amery, Ross and Ronne ice shelves recorded data for longer periods for later downloading during a return visit (e.g. Herraiz-Borreguero, 2016; Arzeno and others, 2014). The British Antarctic Survey and the Naval Postgraduate School pioneered an early attempt at automated through-the-ice moorings as part of the Pine Island Glacier drilling project in 2012–13 and a series of projects on the Ronne and Larsen C ice shelves since then (Stanton and others, 2013; Nicholls, 2018; Hattermann and others, 2021). These moorings variously featured an ascending/descending CTD profiler, a turbulent-flux sensor suite and two-way communications for both data uploading and managing the data acquisition protocol.

The AMIGOS-3 is an augmented version of an earlier system intended for surface and subsurface glacier and ice-shelf observations. The early versions of the AMIGOS stations, used during 2006–18 (Scambos and others, 2013), were deployed extensively in the Larsen B embayment region (e.g. Cape and others, 2015; Wellner and others, 2019), on the Drygalski Ice Tongue in the Ross Sea (Lee and others, 2016) and on icebergs drifting north from the Antarctic Peninsula to the South Atlantic Ocean (Scambos and others, 2008). The stations provide point or profile observations of a wide array of climate, ice and ocean characteristics. Data are uploaded daily by these systems using Iridium modems, several of which could not be revisited due to decreasing ice-shelf stability or late-stage break-up of the host icebergs. The stations

were able to operate well past a typical polar field season. Stations installed on the icebergs documented the changing climate and ice-surface changes as they drifted northward until just before their collapse, strengthening conceptual models of ice-shelf disintegration (Scambos and others, 2009). Stations in the Larsen B region contributed weather data to studies of foehn wind frequency (Cape and others, 2015) and validation of an accumulation model for the Antarctic Peninsula (Van Wessem and others, 2016). These stations did not include ocean or deep ice instrumentation, but did include a temperature profile of the upper firn for melt percolation and seasonal thermal variations (e.g. Scambos and others, 2013).

The AMIGOS-3 incorporates several new components and operational improvements over earlier systems, some of which were deployed on a prototype system installed on the Nansen Ice Shelf in early 2017 (Figure S2 and associated text). That system incorporated an ocean sensor suite and a distributed temperature sensing (DTS) system, installed through a hot-water borehole in the shelf, with goals similar to Tyler and others (2013) and an installation similar to the installation described in Kobs and others (2014). While this system was operational only briefly (see Section 2.7), it proved the value of combining climate, ice and ocean measurements (Lee and others, 2019).

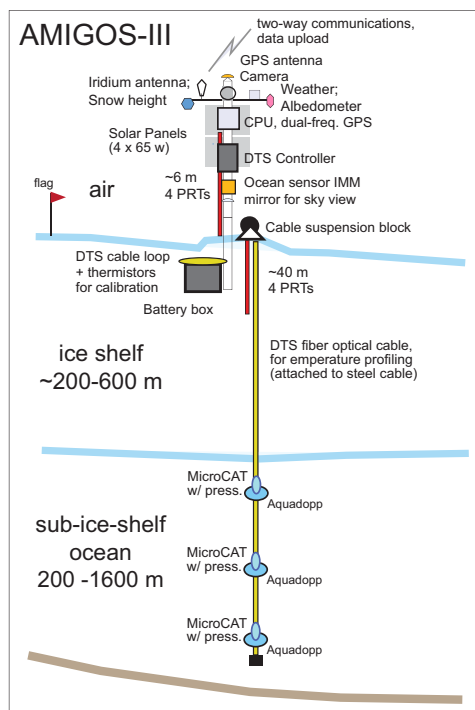
The Thwaites Eastern Ice Shelf (TEIS) AMIGOS-3 systems were initially developed in 2018 and 2019 by a diverse undergraduate engineering team at the University of Colorado’s Space Grant as part of a team-building training exercise (Figure S3). The team pioneered the initial sensor integrations, some sensor calibrations and the first operating code.

Two AMIGOS-3 stations were installed on the TEIS in early 2020, at the ‘Cavity Camp’ (75.0480° S, 105.5858° W) and ‘Channel Camp’ (75.0569° S, 105.4457° W) as part of the Thwaites-Amundsen Regional Survey and Network (TARSAN) project, a part of the International Thwaites Glacier Collaboration (ITGC: [www.thwaitesglacier.org](http://www.thwaitesglacier.org)) providing regular in situ data beginning on 15 January. TARSAN is part of the International Thwaites Glacier Collaboration (see [www.thwaitesglacier.org](http://www.thwaitesglacier.org)). Here, we present an overview of the components, physical structure and software as well as present the available data sets and some of the information they contain regarding the climate, ice and ocean conditions of the TEIS. The summarized quality-controlled monthly weather records for 22 months on the TEIS from the two stations are provided, including the 2020–21 mean annual surface air temperature and pressure (at 5–7 m height above the surface), and average thermistor firn temperatures. Snow accumulation from a sensor and field observations are given. Additional metadata and data visualizations from the GNSS receivers, ocean sensors and DTS are provided to show the data sets’ information content and to present the general conditions present in the TEIS environment.

## 2. AMIGOS-3 processing and software

### 2.1. AMIGOS station overview

Figure 1 provides a tabular listing of the main operating components and sensors for the AMIGOS-3 system, and a diagram and photo of an installation. Further details and photos are provided in the Appendix, Supplemental Information Table S1, and Figures S1 and S2. The station sensor suite includes weather and albedo instruments, an acoustic snow height sensor, a camera, a GPS receiver, multiple ocean sensors—including SeaBird MicroCAT CTD sensors Nortek Aquadopp single-point current meters—and



### AMIGOS-III Main Design Components

#### Structure, Power, and CPU

- CPU: Triton-3 single-board computer, internal ethernet, serial, and USB ports; Linux OS, watchdog function;
- Iridium modem and antenna;
- Aluminum truss tower, 3 m sections, total 9 m installed (1.5 m sub-surface, 7.5 m exposed);
- 6 x 100 amp-hr batteries, 4 x 65 W solar panels

#### Imaging: Surface /Sky condition

- PTZ Camera, full-sky view mirror, flag line

#### Weather / Climate

- Vaisala WXT530 weather station;
- Campbell Scientific acoustic snow-height sensor

#### Ice Motion Sensor

- Dual-Frequency GPS – Topcon B110 receiver, PGA-1 ant.

#### Snow-Firn Energy Balance Sensors

- Albedometer (opposing Apogee SP-212 light meters);
- 4 to 16 thermistors, sub-surface and along tower.

#### Sub-Ice Ocean Sensors

- Silixa DTS laser-stimulated fiber optic thermal profiler;
- SeaBird MicroCAT SBE-37IMP CT sensors, w/ press.;
- Nortek Aquadopp doppler current meters



**Figure 1.** Listing of major components of the AMIGOS station (left) and sketch of an idealized installation of the AMIGOS-3 ice-ocean-atmosphere station (center). Installed AMIGOS-3a at Cavity Camp, TEIS in January 2020 (right). See also Appendix, Table S1 and Figures S1a, S1b and S2.

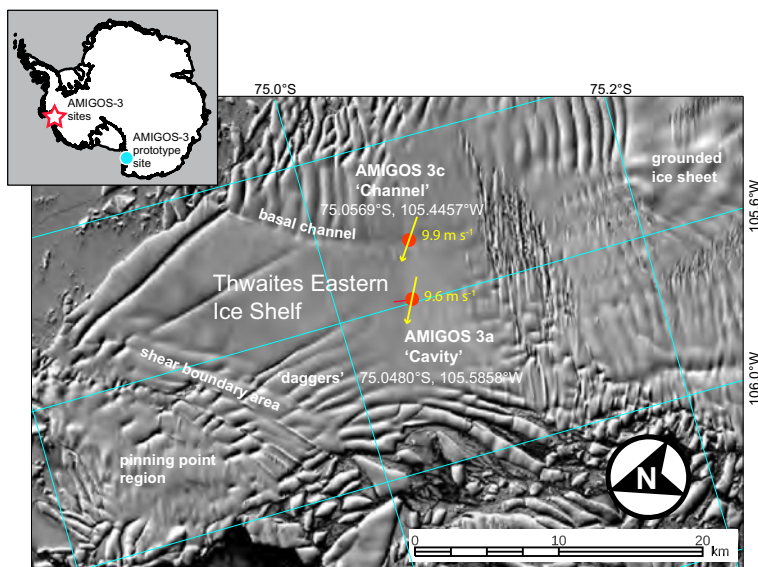


**Figure 2.** Location of the two AMIGOS-3 stations on the Thwaites Eastern Ice Shelf and structural features of the shelf at the time of installation. GPS track of movement of AMIGOS-3a 'Cavity' for January 2020–October 2021 is shown as short red line extending from initial position; total GPS recorded motion of AMIGOS-3c 'Channel' is within the site marker. Yellow arrows indicate mean wind direction for the two sites, with mean wind speed shown next to them. Landsat 8 image (Path 3, Row 113) acquired 31 January 2020. Inset, map of Antarctica showing AMIGOS-3 sites (red star) and the AMIGOS-3 prototype site (cyan dot) on the Nansen Ice Shelf.

a Silixa DTS fiber-optic interrogator and 1600 m fiber cable extending through the snow, ice and ocean beneath the sensor installation. The AMIGOS-3 and prototype installation locations are shown in Figure 2.

## 2.2. Main control board

The Triton-3 CPU board was developed by co-author R. Ross in 2013. (For the following section, see the technical acronym list in Appendix 1.) The main board is designed to have sufficient capability to manage the operating system, coordinate measurements and

interface with the sensors, perform some data preprocessing and file configuration, and then manage the upload of the data within hours of data acquisition. The system can retrieve commands from a remote directory that updates internal operating code, reconfigures the data-acquisition schedule, and supports troubleshooting. The Triton-3 board controller consists of a single commercial system-on-module (SoM) 144-pin SODIMM form factor plugged into a custom carrier board. (A SoM is a small, embedded module that contains the core components of a microprocessor-based computer on a single interchangeable card.) The SoM is an EMAC Atmel ARM9 Jazelle AT91SAM9260 200 MHz processor with 64 MB SDRAM and 64 MB flash memory in a form factor of



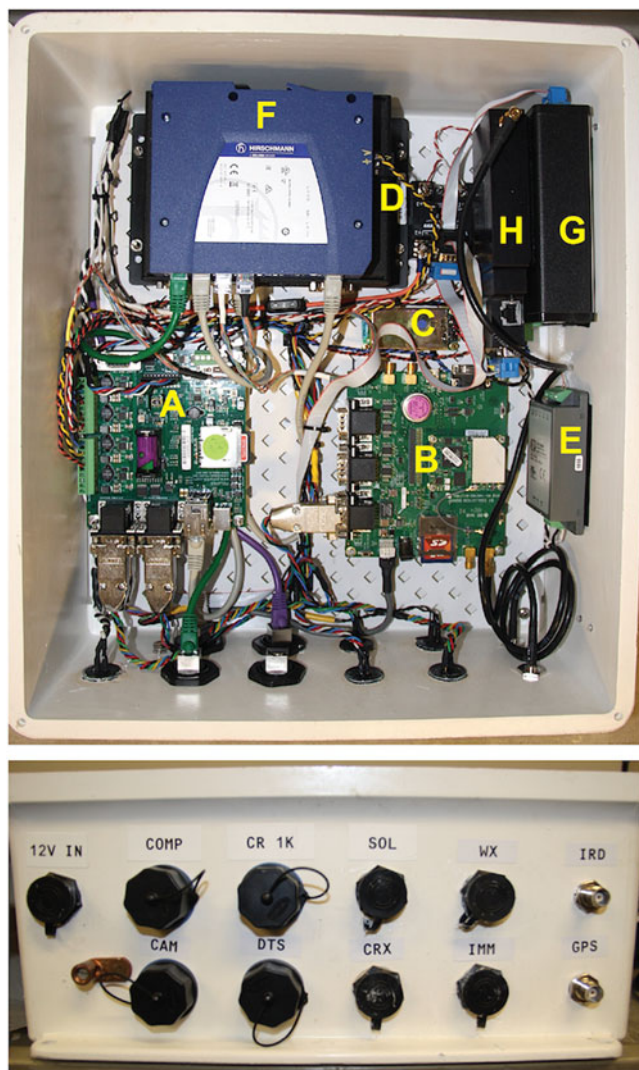


**Figure 3.** Interior of electronics enclosure box (top) and electronics box connector panel (bottom). Top panel has the major electronic components labeled: A, Triton board from Polar66 Engineering (R. Ross); B, TopCon B110 GPS receiver and carrier board; C, SeaBird Inductive Modem Module (IMM) for decoding inductive data transmission from the ocean sensors; D, WinSystems Windows-OS computer for interfacing with the DTS controller; E, a power regulator to provide 12.0 V to the PTZ camera; F, Ethernet hub; G, dial-up router; H, NAL AL3A-R Iridium modem. The white electronics enclosure box is 40 × 30 × 25 cm. Lower panel is an image of the exterior bottom wall of the enclosure, showing the port arrangements for the AMIGOS-3. Port functions clockwise from upper left: power, Ethernet access (for operator), Campbell Scientific CR-1000X Ethernet, four-wire input for albedometer, five-wire input for Vaisala weather data and sensor power; two-wire input from SeaBird inductive coupler circuit (ICC) to IMM; three-wire power input to the CR-1000X; DTS Ethernet; camera Ethernet (with power-over-Ethernet); grounding lug.

67 mm × 38 mm (Table S1a), with a 128 MB serial data flash and an SD/MMC flash card interface. The CPU has very low power requirements (1.5 W run mode, 40 mW sleep mode) and is rated for low-temperature operation (to −40°C).

A custom carrier board was designed for the SoM (hereafter, we refer to this board with the SoM as the ‘Triton-3 board’; Figure 3). The carrier board, measuring 114 × 127 mm, is equipped with an SD/MMC flash card interface, a 10/100 BaseT Ethernet interface, two USB-2.0 host ports, a device port, four RS-232 serial ports and a console RS-232 port, an I<sup>2</sup>C port, four 10-bit

ADC channels, three GPIO-controlled pass-through voltage outputs, seven GPIO-controlled switched voltage outputs (4 × 5 V, 3 × 11.6 V), a single LIN bus and a CAN bus. The carrier board supplies regulated power to the module and has over/under voltage protection, reverse polarity protection, electrostatic discharge protection and a four-channel ADC for measuring input voltage and current draw. In addition, the carrier board includes sensors for temperature, humidity, pressure, a three-axis compass and a three-axis accelerometer, although these were not used in the described installations. The system includes an external PIC microcontroller-based watchdog timer to reset the system in case of software malfunction.

### 2.3. Operating system

The operating system is based on the OpenEmbedded 4.0 Linux distribution, running the Linux 2.6 kernel. A selection of basic cross-compiled utilities and services—such as SFTP, SSH, as well as a collection of scripts, system configurations and Python code—is included, which forms the core of the operating software system. The operating system runs from a high-performance built-in flash drive, while data storage and high-level operations software utilizes the high-capacity removable SD card. The operations software is flexible and configurable, making it easy to adapt to new sensor suite configurations or collection schedules. The central scheduler and supervisor scripts manage the collection and transmission of sensor measurements, data uplinks, and file and sensor maintenance activities. It is designed to be robust to hardware failures and intermittent power. Shared resources (e.g. networking hardware, processing) are managed to avoid conflicts and interactions, and to minimize power usage as much as possible.

### 2.4. Software architecture

The AMIGOS-3 units operate on a daily cycle of two main processes. The first is the *scheduler*, which is generally always running, sequencing the sensor measurements, data uplink periods and sleep/hibernation. The scheduler manages shared resources, powering and operating peripherals, and handling errors/failures in subsystems. The scheduler also monitors the power and initiates a sleep mode for the station when idle or when the supply voltage is low, resuming operation once power is restored. The second major process is the *supervisor*, which is independently triggered twice a day and performs maintenance activities (e.g. archiving logs/data, cleaning queues, stopping/starting the scheduler), system health monitoring and execution of remote commands, software updates, etc.

### 2.5. Sensor and uplink communications

In addition to the main Triton board, the main electronics enclosure includes internal and external communications components: an induction modem for communicating with the ocean instruments; and an Ethernet hub, dial-up router and Iridium modem for data and station-health uploads (Figure 3, Table S1b). Also within the enclosure is a compact computer operating Windows 7 for communicating with the DTS internal operating code. Much of the AMIGOS-3 data are transmitted in near-real-time as Iridium files or messages delivered to a research institution data server via email (with further processing and staging steps taking place there). Larger data files are uploaded via the dial-out gateway and file transfer protocol (FTP). As Iridium uploads are a significant

part of the power budget, a queue of uploads is maintained and sent out in batches as power and connection quality permit.

The AMIGOS-3 stations use a NAL Research Corporation A3LA-R Iridium modem for data uplink via single-burst data (SBD) packets or file transfers using a point-to-point protocol (PPP) gateway connection and FTP. These modems and the present Iridium satellite network provide a nominal data rate of 9600 baud in dial-out mode. Single bursts of up to 2000 bytes can be transmitted quickly and reliably using the SBD protocol, although larger data files are more efficiently transferred using a PPP dial-out connection. To handle connection dropouts, large files are segmented into 10-kB chunks and added to a managed queue to be uploaded using FTP during scheduled dial-out times, typically several times per day. With signal strength variability and transmission protocol overhead, the effective data transfer rate averages empirically to  $\sim 2000$  baud. These dial-out sessions are also utilized by the units to receive and execute command scripts and software updates which are staged to the FTP server by the operator. The AMIGOS-3 station 'picks up' new instructions during dial-out sessions. This approach was taken because of the difficulty in connecting with the system during dial-in, and the power consumption needed to have the AMIGOS-3 system in an Iridium-on mode for extended periods.

## 2.6. Power

The battery box (Figure 4; Table 1b) contains six 100 A-h batteries, a solar power controller and the CR-1000X data logger, which supports the temperature-sensor array and sonic-ranging sensor.

## 2.7. Failure modes

AMIGOS installations have suffered from a variety of failure modes over the  $\sim 15$  years of installation and data collection activities. Other than burial or direct weather-related damage (e.g. tearing off of a solar panel in high wind), most common have been issues with the Iridium communications (using NAL Research Corporation A3LA-XA units) which in earlier installations had issues with low-temperature operation, as determined from long-term outdoor testing in Boulder Colorado. In more recent systems, newer Iridium transceiver units (NAL A3LA-R) and a greater reliance on single-burst-data (SBD) transmissions have largely eliminated this problem. Static electricity build-up and discharge in dry cold high-wind conditions likely caused the failure of a prototype installation of the AMIGOS-3 system on the Nansen Ice Shelf, ending its operation as autumn katabatic winds increased. This is a known and difficult problem in cold polar environments, since effective grounding is difficult.

Environmental events that led to system failure or long-term down time include heavy rime icing and damage from meltwater. Rime icing is a known problem in areas with super-cooled ice fog, such as at or near the summit of a ridge or dome; this can encase the antennas and weather sensors in thick frost, rendering them inoperable. One early AMIGOS station placed on the remnant Larsen B Ice Shelf at Scar Inlet experienced some firn meltwater flooding in 2010, which slowly filled the battery box (despite water resistant seals) and then discharged the batteries when the water level reached the terminals. (The gradual filling was documented by rapidly changing indicated temperatures in the thermistor string as the data logger, housed in the same enclosure, slowly had its contacts flooded, changing the net thermistor circuit resistance).

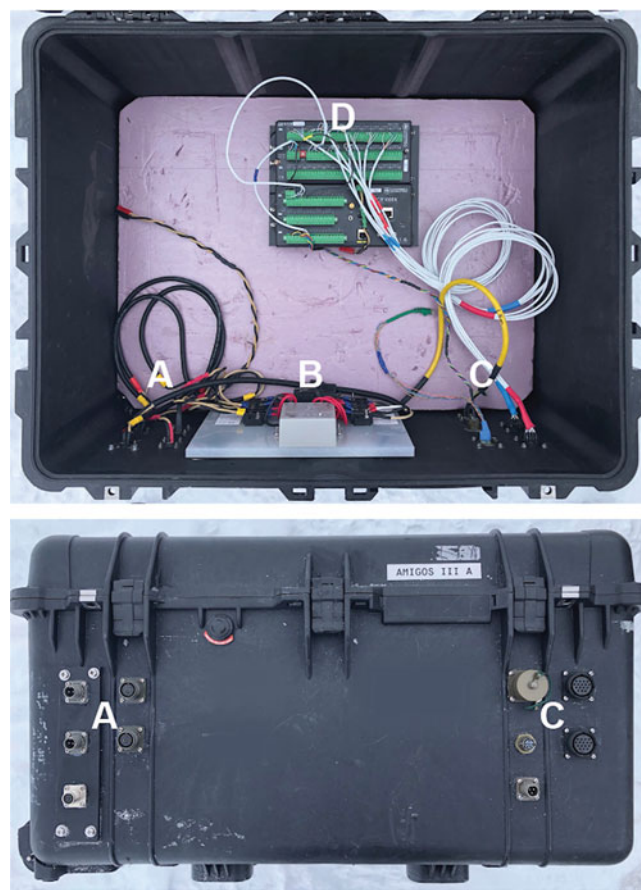


**Figure 4.** Interior of the battery box enclosure (top) and battery box connectors (bottom) for the station in Figure 3. Six 100 A-h batteries fit in the box with 6.5 cm clearance along the connector panel wall. Top and bottom panel labels: A, solar panel input (left side, top two ports), spare power output (lower left side port), main power and DTS power output (right side, two ports); B, solar power controller for battery recharging and system fuses; C, sensor and data input ports (Ethernet port for CR-1000x, top left, snow height sensor input, middle left' power output to DTS, lower left; top right, borehole thermistor cable input; lower right, tower air-snow thermistor cable input); D, CR-1000X data logger for thermistors and snow height measurements. Battery box enclosure is  $80 \times 65 \times 45$  cm.

The acoustic snow-height sensors failed on the two TEIS AMIGOS-3 stations after 10–12 months, likely due to fine snow particles dampening the return signal sensitivity.

## 3. AMIGOS-3 sensor suite

By combining several sensors at one observation site, the AMIGOS stations can provide insight into the relationship between environmental factors, or contribute to evaluating processes and linkages for various forcings or drivers. The AMIGOS-3 sensor group installed on TEIS in 2020 (Figure 1; Table S1) included a camera; weather and snowfall sensors; an albedometer; near-surface snow temperature sensors; a precision GPS; a DTS fiber-optic system for snow, firn, ice and ocean temperature; and ocean instruments (CTDs and current meters).

### 3.1. Optical camera

The camera selected for the AMIGOS-3 at TEIS is a compact point-tilt-zoom outdoor video and still 1080p IP camera that operates on

**Table 1.** Temperature (°C) and pressure (mbar) data for the two AMIGOS-3 sites

AMIGOS-3a (Cavity) Year 2020														
Hourly														
		Jan	Feb	Mar	Apr	May	Jun	Jul	Aug	Sep	Oct	Nov	Dec	
		(363)*	(644)	(693)	(668)	(682)	(657)	(650)	(78)	(515)	(688)	(666)	(704)	
Temp	Max	1.3	1.7	0.4	−2.2	−0.1	−0.2	−0.5	−12.7	−3.9	−4.0	−4.3	−0.2	
	Mean	−4.2	−4.6	−12.1	−18.0	−13.4	−18.0	−15.5	−22.9	−23.1	−15.4	−11.2	−4.7	
	Min	−10.7	−23.3	−31.4	−39.7	−35.4	−34.9	−39.0	−39.2	−43.8	−31.7	−30.6	−12.8	
Press	Max	994.2	994.0	984.3	998.7	996.4	1011.7	1009.6	1002.8	1011.4	1008.7	988.1	983.8	
	Mean	983.9	977.8	968.6	977.1	977.1	977.8	982.5	984.2	978.7	967.3	964.9	969.1	
	Min	967.7	961.7	950.9	954.6	942.2	949.1	947.8	964.3	962.2	940.2	943.3	950.7	
AMIGOS-3a (Cavity) Year 2021														
Hourly														
		Jan	Feb	Mar	Apr	May	Jun	Jul	Aug	Sep	Oct			
		(615)	(537)	(594)	(666)	(702)	(587)	(541)	(32)	(457)	(129)*			
Temp	Max	1.0	−0.3	−1.0	−3.2	−0.9	−2.7	−3.4	−10.0	−7.1	−10.3			
	Mean	−4.4	−7.7	−11.8	−20.6	−23.0	−19.1	−15.6	−23.7	−15.5	−16.3			
	Min	−14.0	−14.7	−22.9	−40.4	−46.1	−34.7	−31.9	−47.2	−26.1	−20.6			
Press	Max	989.3	984.0	982.4	995.3	1015.8	1006.9	995.4	996.2	981.2	972.9			
	Mean	973.7	967.2	970.7	974.8	983.5	980.1	979.7	973.8	963.6	962.5			
	Min	954.0	937.6	938.6	950.0	955.0	951.9	963.4	954.3	937.8	941.2			
AMIGOS-3c (Channel) Year 2020														
Hourly														
		Jan	Feb	Mar	Apr	May	Jun	Jul	Aug	Sep	Oct	Nov	Dec	
		(353)*	(692)	(729)	(674)	(693)	(660)	(634)	(198)	(504)	(692)	(658)	(667)	
Temp	Max	0.4	1.7	0.2	−2.1	−0.2	−0.2	−0.6	−12.7	−3.9	−3.8	−3.3	0.0	
	Mean	−4.2	−4.6	−12.0	−18.7	−13.5	−18.4	−15.2	−20.0	−23.2	−15.6	−11.1	−4.7	
	Min	−11.4	−24.1	−32.1	−41.9	−37.7	−35.5	−40.9	−46.4	−40.5	−34.6	−32.2	−12.8	
Press	Max	994.6	994.2	984.6	999.1	996.8	1012.1	1010.0	1004.9	1011.8	1009.0	988.4	984.1	
	Mean	984.6	978.0	968.7	977.4	977.7	978.2	983.1	973.3	978.9	966.4	965.5	969.3	
	Min	968.0	961.2	950.8	954.2	942.5	949.0	948.1	952.1	962.0	940.3	943.8	950.8	
AMIGOS-3c (Channel) Year 2021														
Hourly														
		Jan	Feb	Mar	Apr	May	Jun	Jul	Aug	Sep	Oct	Annual Average		
		(676)	(620)	(678)	(612)	(678)	(662)	(693)	(463)	(499)	(478)*	(using 19 months)		
Temp	Max	0.9	−0.4	−1.1	−3.3	−0.9	−2.6	−3.1	−8.4	−7.2	−10.5			
	Mean	−4.7	−7.7	−11.8	−21.1	−24.0	−19.6	−15.5	−28.9	−16.0	−16.3	−14.64		
	Min	−15.1	−14.4	−26.0	−44.0	−47.6	−39.4	−35.3	−51.0	−26.7	−22.3			
Press	Max	989.5	984.3	982.8	995.3	1016.4	1007.3	996.3	999.6	981.5	975.5			
	Mean	974.7	967.4	971.0	975.3	984.3	979.2	978.8	977.6	963.6	967.6	973.7		
	Min	954.2	937.9	939.6	950.3	955.8	952.8	959.3	954.2	939.2	942.8			
AMIGOS-3c (Channel) Thermistors (firn temperatures)								AMIGOS-3a (Cavity) Thermistors (air temperatures)						
Hourly, 17 Aug 2020–16 Aug 2021 @ −3.3 to ~−5 m <sup>†</sup>								Hourly, 15 Jan 2020–14 Jan 2021 @+3 to +7 m <sup>‡</sup>						
A	B	C					‘3 m’	‘5 m’	‘7 m’					
(7465)	(7466)	(7465)					(7295) <sup>§</sup>	(7295)	(7295)					
−14.37	−14.15	−14.26					−13.98	−13.78	−13.86					

Note: Data are averaged from hourly reports. Data values in italics indicate the month had too few reports to be included in yearly mean assessment. Data in blue at AMIGOS-3c were used for the 19 month annual assessment.

\*Asterisks next to total hourly reports indicates a partial month.

<sup>†</sup>Range of depth in firn as snow accumulated.

<sup>‡</sup>Initial height above snow.

<sup>§</sup>Partial August data, monthly average used.



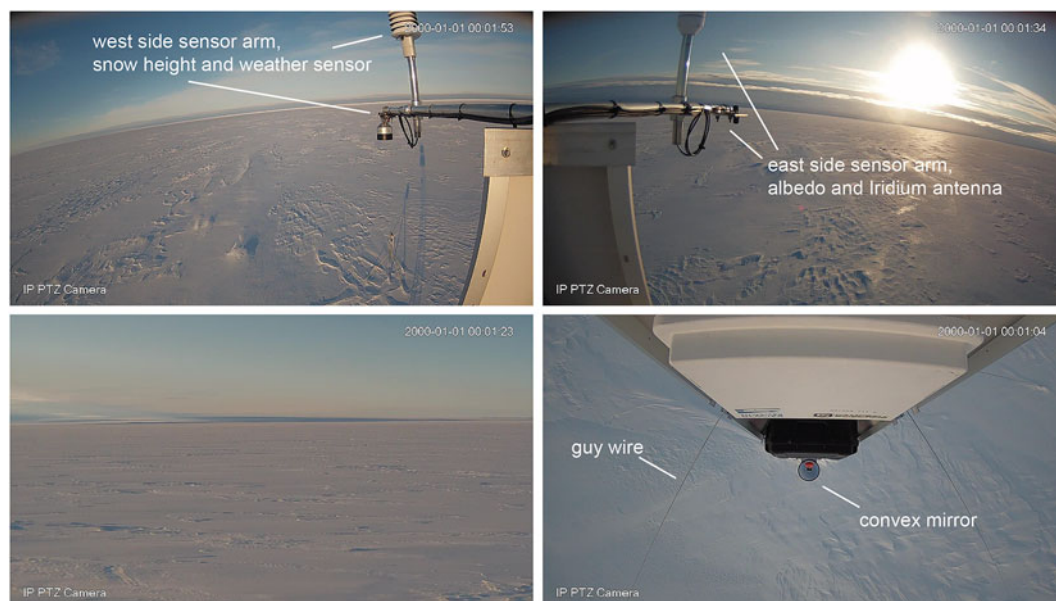


**Figure 5.** Images acquired and uplinked from the AMIGOS-3 installation at the Cavity site on 15 and 16 February 2020, 1 month after installation. Upper images are looking westward (left) and eastward (right) at ~12:12 UTC on 15 February. Weather sensor and acoustic snow-height sensor are in the westward image, along with the upper corner of a solar panel and the sensor cross-pole; Iridium antenna and albedometer are seen in the eastward image. Lower left image is looking southward, also at 12:12 UTC. Lower right image is looking downward at the snow surface on 16 February at 04:12 UTC, with convex mirror and guy-wire supports. Close-up image (not shown) of the mirror can reveal sky and tower conditions.

12 V power (conditioned in the main enclosure to  $12 \pm 0.2$  V), rated to  $-25^{\circ}\text{C}$ , with low-light mode and  $2\times$  optical zoom. The Ethernet-linked camera can record changes in the surroundings (e.g. crevassing, melt pond formation, sastrugi formation and movement) and can take images of snow accumulation stakes or nearby flag arrays, creating a record of snow accumulation and surface roughness (Figure 5). The camera program collects images looking along the sensor arm (in the case of TEIS, oriented east-west) and toward an unobstructed view away from the solar panels (at TEIS, south), as well as down along the tower structure. A convex mirror mounted below the main enclosures enables another view of the tower components and a sky view when the camera is in zoom mode. These are uploaded at reduced resolution daily. Images are typically collected four times per day, excluding polar night, and stored on board at full resolution.

### 3.2. Weather and climate sensors

The AMIGOS station includes an all-in-one weather sensor (Vaisala WXT530). Weather station data for the TEIS installations were gathered hourly based on 10 min of observations just before the UTC hour. The Vaisala weather station records wind speed and direction (using an ultrasonic Doppler ranging method;  $\pm 0.3 \text{ ms}^{-1}$ ;  $\pm 3^{\circ}$  azimuth), air temperature ( $\pm 0.3^{\circ}\text{C}$ ,  $-52^{\circ}\text{C}$  to  $+60^{\circ}\text{C}$ ), humidity ( $\pm 3\%$ ; degrading to  $\pm 5\%$  near saturation) and barometric pressure ( $\pm 1 \text{ hPa}$  under polar conditions).

The sensor suite also includes two additional instruments related to weather conditions and snowfall: an acoustic snow-height sensor (Campbell Scientific SR50A-L) and an albedometer comprising two Apogee Instruments SP-212 hemispheric pyranometers mounted in opposing directions to gather the upward and downward hemispheric reflectance. The acoustic snow-height sensor has an accuracy (after correction for air temperature) of  $\sim \pm 3 \text{ cm}$ ; this accuracy level decreases with falling or blowing snow. Snowfall events (increasing height trend on a

daily basis) and ablation events (decreasing height) are evident in the data. The accuracy for the solar and reflection pyranometers is  $\pm 20 \text{ W m}^{-2}$ . Conditions at TEIS were not as conducive to measuring snow albedo variations as on the Larsen B Ice Shelf glaciers and remnant Scar Inlet ice shelf (Scambos and others, 2013), because frost and snowfall on the TEIS sensors degrade the albedo data time-series. (Snow accumulation is very low on the eastern Antarctic Peninsula, unlike the Amundsen Sea coast; Van Wessem and others, 2016).

Moreover, melt events and snow grain-size evolution are not as frequent or apparent at TEIS as in the Larsen Ice Shelf area. Overall, snow albedo under ideal conditions (high sun,  $>200 \text{ W m}^{-2}$ ; low humidity,  $<85\%$ ) averaged 0.89 with 90% of the variation ranging between 0.80 and 0.98 at the Cavity site in the first year of operation.

A temperature-sensor string, containing eight 1000  $\Omega$  platinum resistance thermometers, is included for determining the firn-temperature gradient, and, when installed along the tower above the surface, is a backup means of measuring snow accumulation and air temperature. Calibration for the temperature sensors before the field deployments, using a chilled circulating alcohol bath and millikelvin calibrated thermometer, established their individual coefficients for converting resistance to temperature with an accuracy of  $\pm 0.02^{\circ}\text{C}$ . The temperature-sensor string can also serve as a calibration reference for the DTS thermal profile. The sensors are designed to be installed at  $-40$ ,  $-20$ ,  $-10$ ,  $-6 \text{ m}$ , and  $+2.5$ ,  $+4.5$ ,  $+6.5$  and  $+8.5 \text{ m}$  relative to the initial snow surface. The string is attached to a Campbell Scientific CR-1000X data logger located in the battery box and includes a reference resistor and an internal temperature sensor.

### 3.3. GPS receiver

The dual-frequency GPS sensor is the TopCon B110 with the TopCon PG-S1 compact antenna (without a ground plane, to

reduce wind drag). The B110 is mounted on a carrier board intended for software development to facilitate simpler coding for GPS operations. The system has proven capable of providing positions precise to within  $\pm 3$  cm with 20–40 min acquisition periods (15 or 30 s epoch acquisitions) and provides precise elevation data as well. GPS data results are discussed in Section 4.4.

### 3.4. Borehole cable sensors

The borehole cable sensor suite comprises four different sensor types: the lower four sensors of the temperature-sensor string, described above; a fiber-optic DTS thermal profiling system measuring both the internal ice and the ocean conditions; and paired sensors for ocean observations, consisting of a SeaBird MicroCAT SBE 37-IMP CTD and the Nortek Aquadopp single-point Doppler-based ocean current meters (see Table S1). The ocean moorings of the AMIGOS-3 stations are arranged as pairs of instruments, with a CTD set 2 m above the current meter instrument.

The AMIGOS-3 DTS system is a Silixa XT-DTS, selected for its low power consumption, fast start-up and 12 V d.c. operation. (The earlier AMIGOS-3 prototype used a Sensornet DTS.) As noted above, a Windows processor in the main control enclosure is needed to boot up the DTS system and run data collection scripts for the units. The DTS laser interrogator is attached to a fiber-optic cable that is connected to a steel cable with small pull-ties set approximately every 2 m. The spatial resolution of temperature measurements along the fiber cable is 0.25 m, but this was generally resampled to 1 m as a way to compress the data, although the 0.25 m rate was uploaded in the 200 m section spanning the ice–ocean interface. The steel cable serves as both a strength member for the ocean instrument string and as a communication conduit for the inductive modem data communications system.

Power requirements for the DTS units were large, up to 20 W for several minutes during start-up. The data collection schedule (and therefore the power consumption) is managed using Iridium downlinked commands. The nominal profile acquisition plan is 6 d<sup>-1</sup>, allowing the recovery of any tidally paced variations when abundant solar power is available, but can be reduced as needed in late winter.

The DTS data require independent measurements or estimates of temperature at several points along the cable for calibration. For the AMIGOS-3 systems, the DTS was calibrated using a simple two-point (slope and offset) calibration to match each of the two SeaBird MicroCAT temperatures collocated on the mooring cables. The MicroCAT measurements were available on a 10 min cadence, and were interpolated to match the time of each DTS measurement. A standard three-point calibration (Hausner and others, 2011) was not used as the thermistors buried with the coiled fiber near the surface exhibited considerable variability, resulting in unstable calibrations. Temperature resolution was  $\sim 0.03$ – $0.04^\circ\text{C}$  at the lowest reaches of the moorings based upon spatial variance estimates over depths of expected uniform temperature.

In the two deployments of the AMIGOS-3 stations on TEIS, the DTS fiber-optic cable was a multi-strand thermal-sensitive steel-jacketed cable between 1200 and 1600 m long, manufactured by Brugg Cables. The cable consisted of a fiber-in-metal-tube (FIMT) system with stainless steel strength elements wrapped over the FIMT and overlain by a polyurethane jacket. Three of the fibers were multimode fibers: two configured as duplexed with a sealed turnaround at the bottom of the cable, and the third as a simplex fiber. One of the four fibers in the cable was an acoustic-sensitive (single-mode) fiber for use with a Distributed Acoustic Sensor

interrogator as part of follow-up field work (not a part of the AMIGOS-3 automated system).

## 4. Climate, ice and ocean conditions from the AMIGOS-3 sites at TEIS

We discuss a few selected scientific results from AMIGOS-3 data to demonstrate the application of multi-sensor in situ observational data. This study also presents final, quality-controlled monthly weather records and accumulation rates for the TEIS region, derived from the AMIGOS-3 observations. A summary of the data sets available from the sensor suite from January 2020 to early 2022 is illustrated in Figure S4.

### 4.1. Weather data summary

The two AMIGOS-3 stations reported hourly weather, including temperature, wind speed, wind direction, humidity and pressure. Temperature and pressure data are summarized in Table 1 (full data are available at the United States Antarctic Program Data Center (USAP-DC, <https://doi.org/10.15784/601549>). Figure 6 illustrates the temperature and pressure data for 22 months at the Channel AMIGOS-3 site, and wind data for both stations. Reporting success through Iridium single-burst-data files is  $\sim 85\%$  (7479 reports out of 8760 h in a year). Data gaps in temperature and pressure data were mainly associated with low station power and failed Iridium SBD uplinks. Wind data were affected by rime and heavy snow on the sensor, particularly in three multi-day periods, May 2020, July–August 2020 and July 2021. Wind speeds  $> 80 \text{ m s}^{-1}$  were deleted as invalid, as extreme and abrupt (i.e. suspect) wind speed changes sometimes preceded long periods of rime obstruction of the sensor ( $\sim 9\%$  of the reported data; sensor limit is  $99.9 \text{ m s}^{-1}$ ). Camera images of the Vaisala sensor in May and July 2020 showed semi-persistent rime accreted on the lower upwind side of the Vaisala but not at the level of obstructing ventilation. A gap in wind direction measurements between bearing 355 and 0 is inherent to the Vaisala sensor.

Air temperatures at the sites ranged from  $+1.7^\circ\text{C}$  (08 February 2020) to  $-51.0^\circ\text{C}$  (17 August 2021). The mean annual air temperature from the Vaisala sensor at the AMIGOS-3c Channel site is  $-14.64 \pm 0.05^\circ\text{C}$  (February 2020–October 2021). The AMIGOS-3a Cavity station does not have an annual mean temperature reported because neither of the August months had sufficient data. In total, 12 184 measurements were made, averaged by month, with monthly measurement counts ranging between 729 and 463; individual air temperature measurements have a precision of  $\pm 0.3^\circ\text{C}$ . This is a compiled annual cycle using 19-months of monthly averages, combining pairs of calendar months where 2 months of good data are available. To be included in this average, a data month had to have  $> 20$  days with measurements, and  $> 450$  hourly measurements. We assessed the potential for solar heating of the unshaded Vaisala temperatures and found that the effect on the mean temperature, even in December and January, is negligible due to the infrequency of low wind speeds (Figure S5 and text). Vaisala sensor heights above the snow ranged from 6.5 to 4.5 m (see Section 4.2).

Separate from the Vaisala measurements, the thermistor-derived annual average air temperature (unshielded but wrapped in reflective foil) ranged from  $-13.78$  to  $-13.98^\circ\text{C}$  at three heights above the snow; these measurements were likely affected by solar heating and rime icing. Average subsurface snow temperature at AMIGOS-3c (at depths of 3.3–5.0 m) is  $-14.26 \pm 0.11^\circ\text{C}$ .



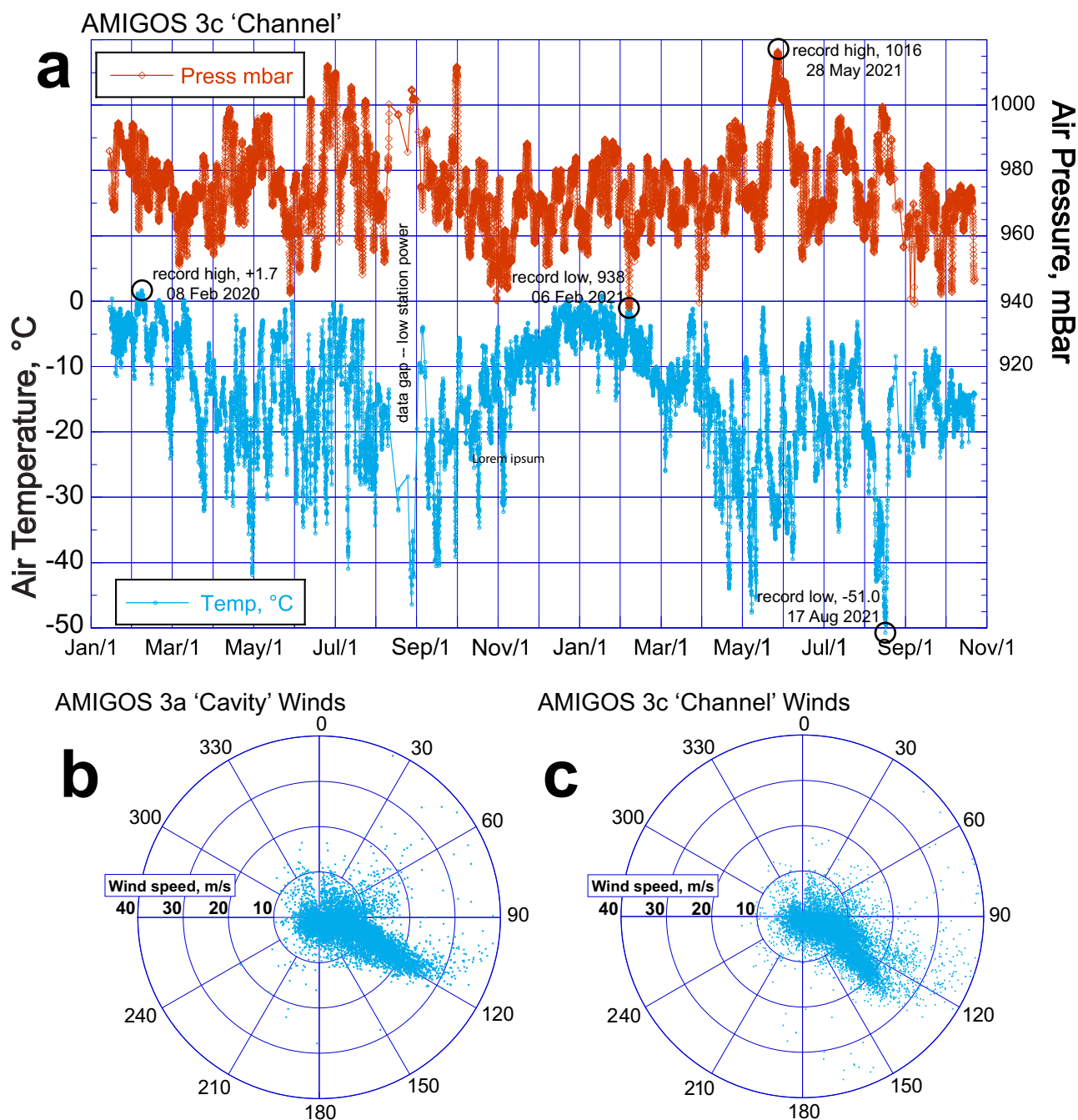


**Figure 6.** (a) Air pressure (red) and air temperature (blue) hourly record for Channel AMIGOS-3c site ( $75^{\circ}03.12' \text{ S}$ ,  $105^{\circ}26.65' \text{ W}$ ) for 16 January 2020–to 22 October 2021, with extremes in conditions labelled. (b) and (c) Wind rose diagrams for Cavity AMIGOS-3a site ( $75^{\circ}02.57' \text{ S}$ ,  $105^{\circ}35.03' \text{ W}$ ; 16 January 2020–07 October 2021) and Channel AMIGOS-3c.

The annual average air pressure was 973.7 mbar (using the 19 month averaging scheme), with individual measurements ranging from 937.6 mbar (at the Cavity site) to 1016.4 mbar (at the Channel site). The individual measurement accuracy of the Vaisala sensor air pressure is  $\pm 0.5$  mbar. Pressure data were very similar between the two stations, with monthly means within 1 mbar and monthly high and low pressures within 1.5 mbar for months with  $>350$  hourly measurements (except July 2021).

Mean wind speed as reported by the stations is  $9.6 \text{ m s}^{-1}$  at Cavity (9943 valid measurements) and  $9.9 \text{ m s}^{-1}$  at Channel (11 531

valid measurements); however, there are two significant gaps in the wind data in late May and much of August 2020 due to snow or rime covering the sensor (this was confirmed by the camera data). Wind speeds are lowest in December and January, with few strong events ( $>25 \text{ m s}^{-1}$ ). Wind direction at the two stations was relatively constant from the southeast, at  $112^{\circ}$  at the Cavity (52% of observations were between  $100^{\circ}$  and  $125^{\circ}$ ) and  $125^{\circ}$  at the Channel (52% between  $110^{\circ}$  and  $135^{\circ}$ ), with wind speeds  $<30 \text{ m s}^{-1}$  for more than 98% of observations. However, a few extreme wind events were observed, and deemed valid because of commensurate

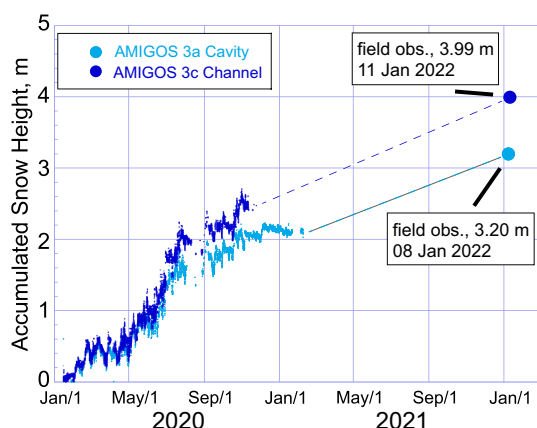


**Figure 7.** Snow height for the two AMIGOS stations for 2020 and 2021.

air pressure changes and multiple similar wind speed measurements over several hours, with peak speeds  $>60 \text{ m s}^{-1}$  at both stations during the winter or early spring periods. The strong directionality of the winds at both stations is consistent with polar easterly and katabatic orientations (e.g. Caton Harrison and others, 2022; Figure 6).

#### 4.2. Snow height and annual accumulation

Snow-height data provide a check on model estimates of net accumulation, and information on the seasonality of snow-fall (Figure 7). The acoustic snow-height sensors failed on both stations after 10–12 months. The data were corrected for air temperature as measured in the same hour by the weather instrument. (Air temperature changes the speed of sound in the sonic height measurements.) A data quality index is reported for each acoustic height measurement. A field measurement of snow height to the sensors was acquired during a brief revisit to the AMIGOS sites in early 2022, extending the total accumulation record to 2 years. Accumulation at the AMIGOS-3a Cavity site was overall  $\sim 20\%$  lower than at the AMIGOS-3c Channel site, possibly because of the setting of the Channel site a few meters lower than the surrounding ice-shelf surface. Although the extent of hourly data acquisition is short (see Figures 7 and S1), it seems that accumulation is highest in late autumn and winter, and lower in the spring and summer months (consistent with the climatology reported in MacLennan and Lenaerts, 2021). The stations recorded accumulation and other weather data during a series of atmospheric-river events in early February 2020, accounting for  $\sim 19\text{--}25 \text{ cm}$  of snow accumulation (MacLennan and others, 2023). Assuming an average snow density of  $450 \text{ kg m}^{-3}$ , the net annual accumulation is  $\sim 0.72\text{--}0.90 \text{ m w.e.}$  (AMIGOS-3a and -3c, respectively).

#### 4.3. Snowfall variations with wind direction

Snowfall rates varied systematically with wind direction (Figure 8). Combining wind speed and direction with smoothed (12-hour running mean) averages of the acoustically determined snow height, a pattern of high snowfall rates with northeasterly winds and low snowfall or ablation conditions with southeasterly winds is seen. Valid observations were available  $\sim 65\%$  of the time. High snowfall rates occur more frequently at the Cavity site than at the Channel site, yet total accumulation at Channel is  $\sim 20\%$  higher

due to far more periods of low snow accumulation (56% of observations), suggesting accumulation under blowing snow conditions rather than precipitation. At the Cavity site, deflation and compaction occurred more frequently (50% of observations).

#### 4.4. GPS data summary

The GPS receivers on the AMIGOS-3 stations were operated at varying rates, between 1 and  $10 \text{ d}^{-1}$  acquisitions of 30 s epoch data for 20 min (40 epochs each acquisition; see Figure S1). The AMIGOS-3a Cavity GPS operated with few gaps from 16 January 2020 to 30 September 2021. Additional data were acquired intermittently in 2022 after a partial repair of the station in January 2022. The AMIGOS-3c Channel GPS also began to transmit data on 16 January 2020, and operated without gaps until it failed on 07 August 2020.

Initial positions of the two stations were  $75.0480^\circ \text{ S}$ ,  $105.5858^\circ \text{ W}$  for AMIGOS-3a Cavity, and  $75.0569^\circ \text{ S}$ ,  $105.4457^\circ \text{ W}$  for AMIGOS-3c Channel, separated by 4.1 km. The Cavity GPS antenna has a mean initial elevation of 26.4 m above the WGS84 ellipsoid (55.3 m above the EGM2008 geoid), and the Channel antenna was 21.5 m above WGS84 (50.6 m above the geoid). Initial flow speeds at the two sites were similar,  $1.74 \pm 0.02 \text{ m d}^{-1}$  ( $636 \pm 8 \text{ m a}^{-1}$ ) and  $1.64 \pm 0.03 \text{ m d}^{-1}$  ( $600 \pm 11 \text{ m a}^{-1}$ ), respectively, averaged over a 20 day period shortly after installation (25 January–14 February 2020). Flow direction was initially  $004^\circ$  at the Cavity site (bearing  $258^\circ$  grid),  $003^\circ$  at Channel ( $257^\circ$  grid), very similar to the satellite-derived flow directions in Alley and others (2021) for the mid-shelf area. Flow speed increased at the Cavity site to  $1.94 \pm 0.025 \text{ m d}^{-1}$  ( $708 \pm 9 \text{ m a}^{-1}$ ) after 1 year, and was  $2.20 \pm 0.005 \text{ m d}^{-1}$  ( $803 \pm \text{m a}^{-1}$ ) during 01–20 September 2021. An inflection in the acceleration rate appears to begin in early June 2020; acceleration at the Cavity site was  $0.36 \text{ mm d}^{-2}$  between January and April 2020, but increased to  $0.923 \text{ mm d}^{-2}$  from September 2020 to September 2021. Satellite images suggest that the cause was related to reduced total shear resistance and an increasingly well-defined and fractured shear margin between the shelf ice and the pinning point areas to the north of the AMIGOS sites. (Wild and others (2022) discussed the gradual development of this shear zone.) Flow direction at the Cavity site turned slightly eastward (as measured by the moving station) during 2021 and was  $015^\circ$  true in September 2021 ( $270^\circ$  grid).

The GPS units appear to record flow-speed variations related to several minor changes in the structure of the TEIS and its connections to the rest of Thwaites Glacier and the pinning point ice rumple at its northern edge (see also Alley and others, 2021; Wild and others, 2022). In the first 4 months of 2020, when both GPS systems were operating, there were two periods when minor oscillations in flow speed occurred at both stations ( $\sim 0.1 \text{ m d}^{-1}$ ; labeled 'A' and 'B' in Figure 9). While variations in flow speed at other times generally did not correlate (and are likely due to wind effects on the towers, or noise in the data), during these two larger variations, flow speeds between the two stations had a Pearson's correlation coefficient ( $r$ ) of  $>0.9$ . Examining satellite images of the region during these periods (e.g. see <https://thwaitesglacier.org/about/science>) suggests they are related to intermittent connection and disconnection between the main ice shelf and rotating blocks along the disaggregating western shear margin adjacent to the central Thwaites outflow. The events were largely variations along flow, with very little change in flow direction.

A significant change in the acceleration of the ice shelf occurred sometime during the winter of 2020, within a GPS data gap due to

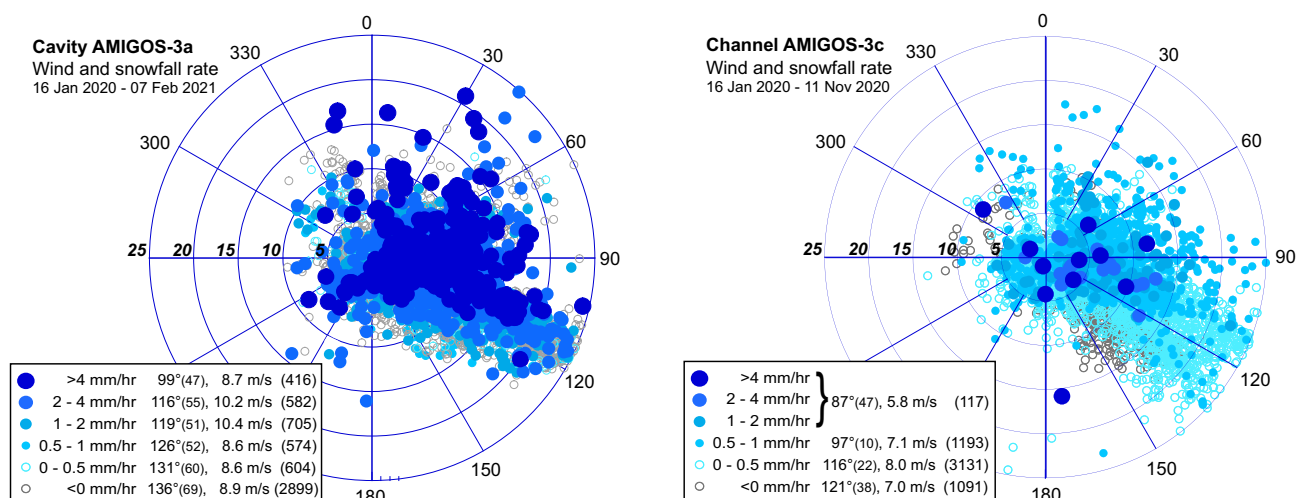


**Figure 8.** Wind rose with snowfall rate (color and symbol size) for AMIGOS-3a Cavity and -3c Channel. Hourly wind speed (10 min means at top of each hour) for the date ranges shown, with smoothed (12 h running mean) snowfall rate indicated by symbol color and size. Number of observations (Cavity, 5780, Channel 5532) is fewer than the number of hours due to gaps in data transmission or frost on one or both sensors used for each graph. Mean wind vectors for snowfall rate bins are shown in the inset tables, with standard deviation of direction in degrees, mean wind speeds and total number of observations.

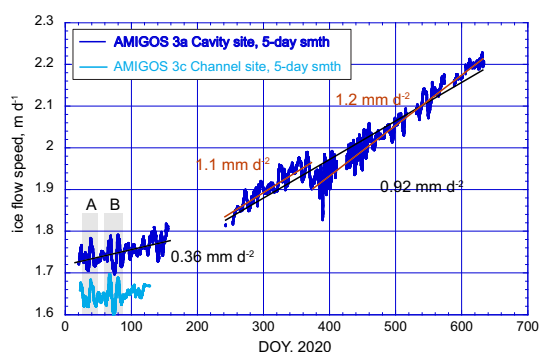


**Figure 9.** Ice flow speed for AMIGOS-3a Cavity (blue) and AMIGOS-3c Channel (cyan) determined by dual-frequency GPS data. Speed determinations were smoothed using a 5 day running mean. The periods of correlated speed variations, labeled A and B, are discussed in the text.

low battery power. Flow acceleration increased from  $0.36 \text{ mm d}^{-2}$  for the first 6 months of 2020 to  $\sim 1 \text{ mm d}^{-2}$  thereafter. Satellite images indicate that shearing of the northwestern part of the ice shelf past the grounded 'pinning point' ice associated with the ice rumple became more concentrated within a few rifts along the ice-shelf edge at this time. A break in the acceleration of the ice shelf near the AMIGOS stations occurred early in 2021, possibly associated with new cross-flow rift extension and widening downstream of the stations (Wild and others, 2024, in press).

Maximum ocean tidal range, as determined by the sub-daily height variations of the Cavity and Channel GPS, is 1.6 m (Figure 10). An analysis of the correlation between the AMIGOS-3a vertical displacement and the CATS2008 model (Howard and others, 2019), with corrections for the inverse barometer effect (IBE; Padman and others, 2003) based on both AMIGOS stations' air-pressure variations and those from the Thurston Island AWS, showed a mean difference of  $\pm 17 \text{ cm}$  (Wild and others, 2022). Both stations showed a steady decline in elevation over time, at a rate of  $\sim 1 \text{ m yr}^{-1}$ , as accumulation buried the stations and weighted the ice shelf, a trend that was removed before comparison with

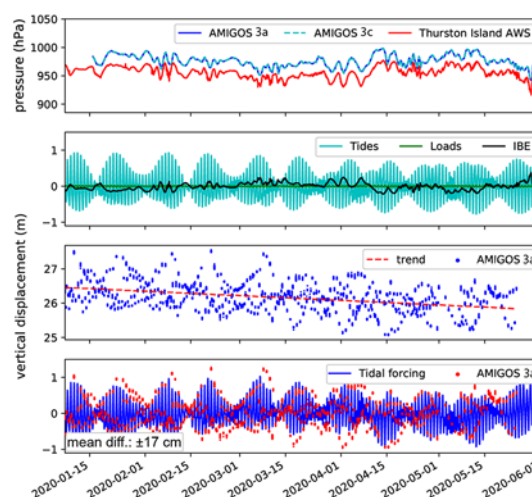


**Figure 10.** Air pressure, ocean and load tides, and inverse barometer effect (IBE), GPS elevation trend with time, and comparison of the corrected tide model (CATS2008 with load and IBE added) with the observed GPS vertical positions for the first five months of AMIGOS-3a Cavity GPS operation.

the tide model. Given the cool ocean temperatures at the ice base (see Section 4.6), and the similarity between accumulation-driven weighting and the elevation decline, we infer that basal melting is a small component of this elevation decline.

#### 4.5. Ocean data summary

The three pairs of ocean sensors used for the TEIS AMIGOS-3 units were intended to be arranged just below the base of the ice shelf, at a mid-depth location and near the seabed. Unfortunately, differences in the spool meters for the science instrument winch and the drilling winch led to the systems being installed several meters higher than intended. With this, the upper sensor pairs were actually installed 2–7 m above the ice base and within the refreezing borehole. The final depths below sea level of the instrument



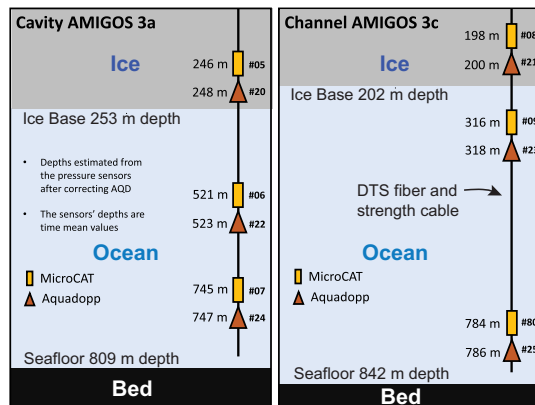


**Figure 11.** Configuration of ocean string instruments in the two AMIGOS-3 moorings. Ice-base depths were estimated from Distributed Temperature Sensing (DTS) fiber-optic cable data; seafloor depth was determined by an initial CTD profile run that was lowered to the seabed. The depths of the ice base reflect conditions in the first few months after AMIGOS installation. AOD stands for Aquadopp.

pairs were determined from the pressure sensors on the CTDs and current meters (Figure 11).

The goal of the TEIS AMIGOS-3 stations was to determine the depths of the different ocean water types known to be in the Amundsen region, among them, Winter Water (WW) and modified Circumpolar Deep Water (mCDW; see Wåhlin and others, 2021). We also sought to determine meltwater content in the mCDW or mixed water types, and the flow directions at different depths, as part of assessing ice–ocean interaction in this part of Thwaites Glacier (Dotto and others, 2022).

Oceanographic data were acquired every 10 min from the CTDs and every hour from the current meters. The units communicated with the surface station through an inductive modem, and the data uplinked with other data parcels via Iridium. This was subject to gaps due to low station power or failure of the station inductive modem system. However, the units had onboard data storage as well, and for the CTDs a full record (January 2020–January 2023) was later recovered by direct communication over the inductive modem. For the current meters, only the preceding 48 hourly records were stored, so that record is more intermittent (although a few records were obtained from the Cavity current meters in January 2023).

An overview of the CTD data, presented as a conservative temperature–absolute salinity diagram, for both stations for the 140 days following installation is shown in Figure 12, along with data from an autonomous underwater vehicle (a Hugin AUV, *Ran*; Wåhlin and others, 2021) that also sampled the sub-ice-shelf cavity waters on 28 February and 5 March 2019 (a year before the AMIGOS’ installation). The characteristics of mCDW in the TEIS cavity, sampled by the deep CTDs in both AMIGOS-3, form a tight pattern centered near  $1.0^{\circ}\text{C}$  and  $34.85\text{ g kg}^{-1}$ . Mid-cavity water, measured at 521 m at the AMIGOS-3 Cavity, shows mixing between the mCDW and WW. The water higher in the water column (bottom left in Figure 12) is aligned parallel to the  $27.4\text{ kg m}^{-3}$  isopycnal (gray thin line). The reference composition for local WW shown in Figure 12 was derived from near-surface seal-tag measurements (Dotto and others, 2022).

Overall, the oceanographic data set indicates a relatively low meltwater content for this first period of data gathering beneath the TEIS, implying that the sampled waters had not been near

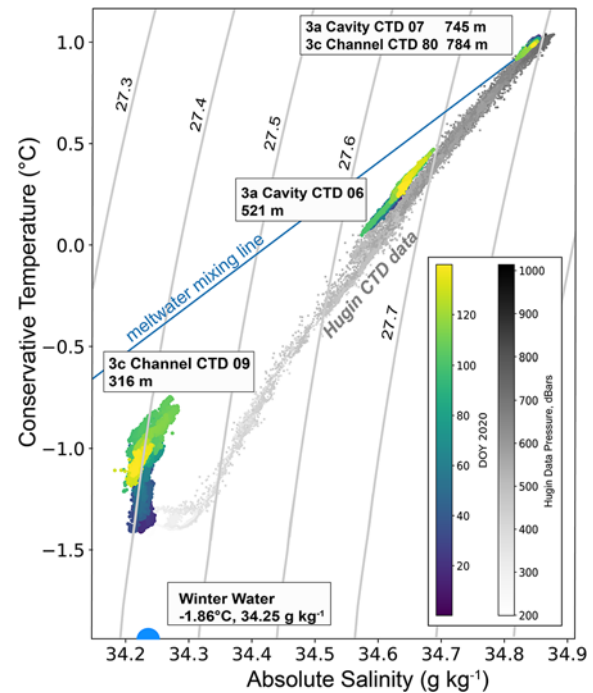


**Figure 12.** Conservative temperature–absolute salinity diagram for the combined CTD data sets from both AMIGOS-3 stations under the TEIS. The meltwater mixing line is derived from Gade (1979) using the mean composition of the mCDW in the upper right. Data from the Hugin AUV deployments during the February 2019 cruise of the RV N.B. Palmer are shown in gray with gray tone scaled to depth of the measurement (Wåhlin and others, 2021). The composition of Winter Water shown here is based on seal-tag observations from 2019 (Dotto and others, 2022).

sites of melting beneath TEIS, nor had the sub-ice cavity received water that had experienced significant melting from the Pine Island Glacier cavity (e.g. see Dotto and others, 2022; Zheng and others, 2022). Mixing between the mCDW and WW accounts for most of the spread in the mid-depths of the cavity shown by CTD 06 in Figure 12. However, the mixing in the upper levels of the ice-shelf cavity, from CTD 09 ( $\sim 100\text{ m}$  beneath the ice-shelf base at Channel mooring), appears to be the result of secondary mixing of the mCDW, WW and varying amounts of fresher water derived from basal melt elsewhere in the region, as seen by its proximity to the meltwater mixing line (Gade, 1979). The distribution of the 140 day measurements from CTD 09 along an isopycnal (i.e. constant density) line suggests that at this level, waters have low stability and density compensation between temperature and salinity, which possibly reflects convective processes.

#### 4.6. Distributed temperature sensing

DTS laser interrogator systems (Silixa XT, Silixa LTD., Hertfordshire, UK) were integrated into both AMIGOS-3 sensor systems and connected to two  $\sim 1600\text{ m}$  fiber-optic cables that were installed in the boreholes and connected to the main steel cable for the ocean moorings. Because the depth to the seabed was  $<850\text{ m}$ , excess fiber cable was coiled just above the AMIGOS-3 battery boxes and buried, initially  $\sim 1\text{ m}$  below the surface. A short stretch of the cable runs  $\sim 50\text{ cm}$  higher between the battery box and the adjacent borehole entry,  $\sim 3\text{ m}$  at the AMIGOS-3a Cavity site, but  $\sim 25\text{ m}$  for the AMIGOS-3c Channel site.

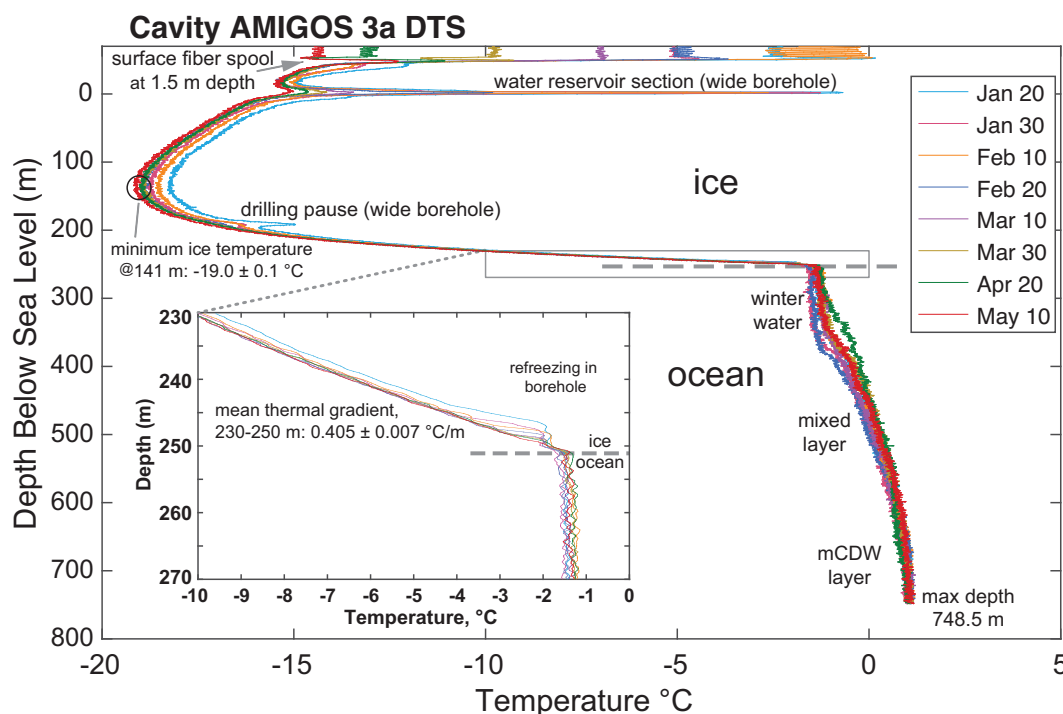


**Figure 13.** DTS temperature profiles for selected days in the first 140 days of 2020 following hot-water drilling of the borehole. Inset, close-up of the ice–ocean boundary.

Power requirements for the DTS units were large (up to 20 W for several minutes during start-up). Data collection by the units was managed using Iridium downlinked commands based on power availability. The nominal profile acquisition plan was 6 d<sup>-1</sup>, when abundant solar power was available, but this was reduced to 1 d<sup>-1</sup> or 1 week<sup>-1</sup> during late autumn and winter (30 April–01 October). The units provided data for 19 months with some outages (see Figure S1). Calibration of the DTS signals made use of the two CTD sensors in the water column via a simple two-point (slope and offset) calibration method.

Thermal profiles through the ice column in the borehole adjusted significantly over the first 140 days of operation but revealed the basic conditions of the ice and ocean (Figure 13). Throughout the firm and ice section of the borehole (below the near-surface spool of cable), the borehole temperature decreased as the effects of the hot-water drilling diffused. Seasonally varying conditions in the upper firm were observed in the upper borehole but were of limited use because the upper borehole likely retained air pockets after burial by drifted snow. The minimum temperature of the ice shelf was recorded at 141 m below sea level,  $-19.0 \pm 0.1^\circ\text{C}$  at the Cavity, and at 118 m below sea level,  $-18.4 \pm 0.1^\circ\text{C}$ , at the Channel by mid-May (~140 days since drilling). Below that depth, temperatures increased rapidly to the base of the ice shelf. In the 15 m just above the respective ice bases, the thermal gradient was very steep,  $0.405 \pm 0.007^\circ\text{C m}^{-1}$  at the Cavity site, and  $0.385 \pm 0.008^\circ\text{C m}^{-1}$  at the Channel site.

The time series of fiber-optic temperature data in the ice-shelf ocean cavity through the first 140 days (Figure 14) shows the general warming of the water column with depth, and the high melt potential of the deepest 100+ m, where temperatures of  $+1.1^\circ\text{C}$  are present. Variations in the middle of the water column are likely related to eddies, or possibly to convection as suggested by the constant density of the mid-depth water in the CTD data (Figure 12). In the upper water column, the coolest layers thin

significantly during the first few months at both sites, and the uppermost 40 m in the Channel water column is near the pressure melting point,  $-1.7^\circ\text{C}$ . However, in both columns, there is a thin (2–3 m) layer that is at the pressure melting point adjacent to the ice base. This layer appears to insulate the ice shelf from basal melting, which is observed to be very small in the full DTS time-series (and in fact is hard to discern in the vicinity of the boreholes because of refreezing above the ice base; Dotto and others, 2022) and in phase-sensitive-radar time-series measurements (1–4 m a<sup>-1</sup>; Wild and others, 2024 submitted). At the top of the profiles, the freezing of the lowest section of the borehole progresses through the first several weeks after the hot-water drilling.

#### 4.7. Sub-ice-shelf ocean current data summary

The four functional single-point current meters at the two moorings measured ocean current flow for ~14 months in total out of the 22 months the stations were active. Gaps in this record (summarized in Figure S4) are due to problems with the inductive modem receivers on the two stations, likely initiated by static build-up on the station during storms. Remarkably, the modems reacquired transmitted data after deep power cycling in late winter as battery power fell below the operating threshold for the stations, and then recovered as solar charging increased in September.

Ocean current data for the four different depths are summarized in Table 2. Ocean flow speeds were generally low and highly variable at all levels measured. Ocean flow directions were also highly variable, but water movement was generally to the south-west at all measured depths. None of the layers showed a consistent correlation with tidal cycles as measured by the GPS units on the stations. Over the entire record, average flow speeds were higher for the shallower two sensors, in the WW and at the thermocline

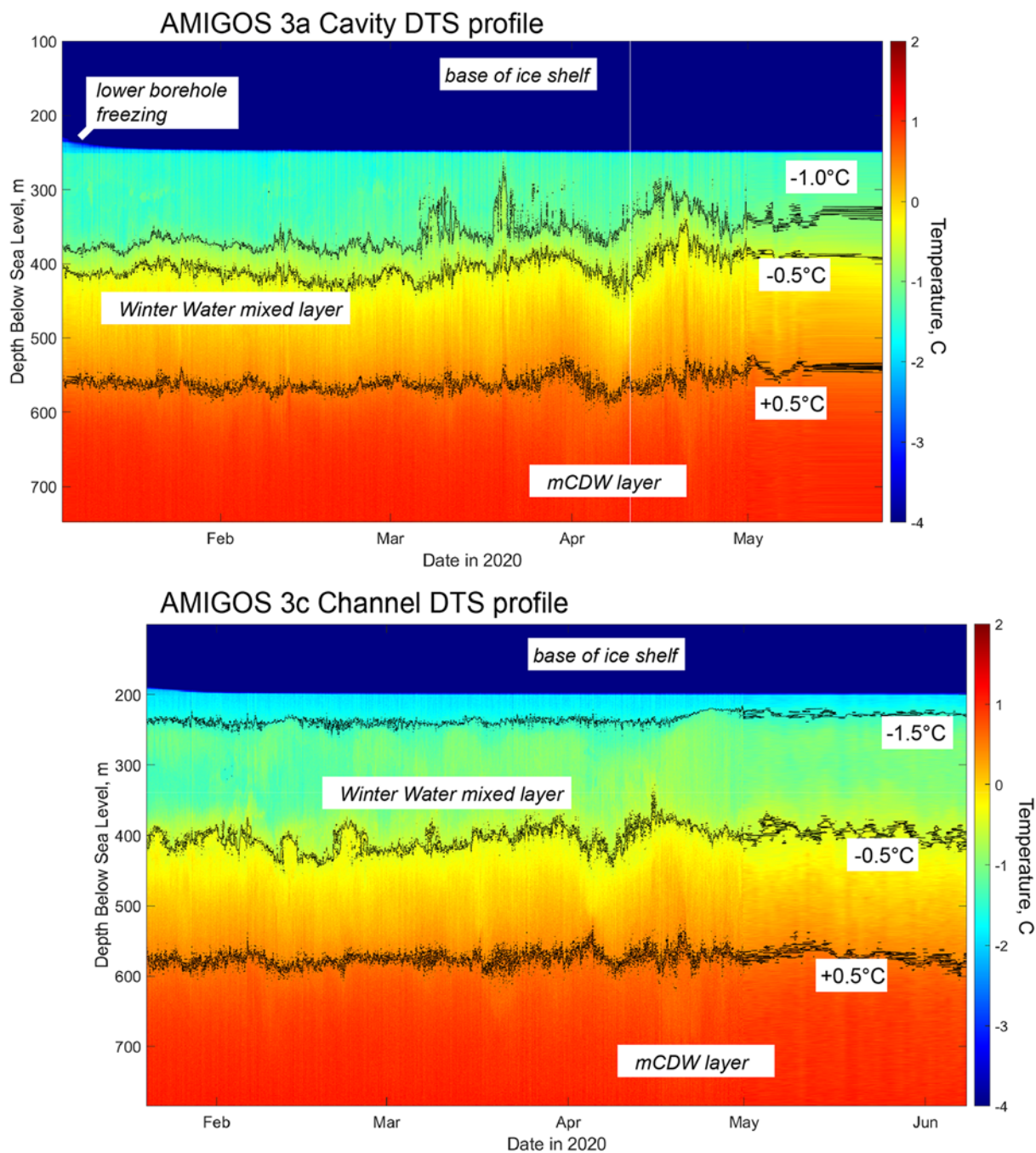


**Figure 14.** Time series of DTS profile data through the ocean column and base of the ice shelf for the first few months of data acquisition. The two graphs are shifted to align the dates. Note that the uppermost ocean layer at the Channel site is cooler than Cavity, with temperatures below  $-1.5^{\circ}\text{C}$ . The  $-1.0^{\circ}\text{C}$  contour is not shown at the Channel for clarity (it is highly contorted).

(318 and 523 m, respectively). The variability in flow speed and direction means that the average net drift distances were small:  $\sim 37 \pm 75 \text{ km mn}^{-1}$  for the 318 m depth in WW layer;  $52 \pm 106 \text{ km mn}^{-1}$  at the 523 m thermocline layer; and just  $16 \pm 39 \text{ km mn}^{-1}$  and  $5 \pm 44 \text{ km mn}^{-1}$  in the mCDW layer at 747 and 786 m depth, respectively.

The bimonthly averages (and a 1 month average for March 2021) of ocean currents were calculated to assess variations in flow speed at a temporal scale that would indicate significant net transport variations. Speeds in the thermocline increased in the late

summer and autumn months and were high in the WW layer also in early 2021. For January–February of 2021, ocean drift speeds were the highest of all periods assessed at all layers. We note this was a period of low sea ice cover in the Amundsen Sea Embayment, possibly enhancing wind traction on the ocean surface. Dotto and others (2022) observed that persistent fast ice in Pine Island Bay led to an accumulation of meltwater-enriched seawater in the upper ocean layer. The buoyancy effects of this accumulation as it moved westward into the TEIS cavity may also be a factor here.



**Table 2.** Ocean drift speeds in 2020 and early 2021 as measured by the Nortek Aquadopp sensors on the two AMIGOS-3 stations on TEISUnits of the entries are shown in the 'All Obs' (all observations) column

	All Obs	Feb–Mar 2020	Apr–May 2020	Jun–Jul 2020	Sep–Oct 2020	Nov–Dec 2020	Jan–Feb 2021	Mar 2021
AMIGOS-3c Aqd23 318 m Channel Site (upper) <b>Winter Water</b> (9094 obs)	$1.4 \pm 2.9$ cm s <sup>-1</sup> 209° (9094 obs)	$0.6 \pm 2.5$ 311° (1412)	$0.6 \pm 2.3$ 357° (1379)	$1.9 \pm 3.1$ 201° (1297)	$1.2 \pm 2.1$ 213° (1194)	$1.6 \pm 2.2$ 213° (1320)	<b><math>4.6 \pm 2.5</math></b> 199 ± 42° (1290)	$2.0 \pm 2.1$ 203° (650)
AMIGOS-3a Aqd22 523 m Cavity Site (upper) <b>Mixed Layer</b> (6976 obs)	$2.0 \pm 4.1$ cm s <sup>-1</sup> 214° (6976 obs)	<b><math>3.1 \pm 2.2</math></b> 241° ± 49° (1214)	<b><math>3.6 \pm 3.4</math></b> 246° ± 66° (1181)	(insufficient data)	$0.1 \pm 5.1$ 343° (1141)	$1.7 \pm 2.1$ 183° (1319)	<b><math>5.0 \pm 3.9</math></b> 152 ± 58° (1185)	<b><math>1.8 \pm 1.8</math></b> 134° (542)
AMIGOS-3a Aqd24 747 m Cavity Site (lower) <b>mCDW layer</b> (6963 obs)	$0.6 \pm 1.5$ cm s <sup>-1</sup> 223° (6963 obs)	$0.1 \pm 1.4$ 217° (1214)	$0.6 \pm 1.6$ 226° (1183)	(insufficient data)	$0.2 \pm 1.5$ 222° (1145)	$0.5 \pm 1.2$ 229° (1317)	<b><math>1.5 \pm 1.5</math></b> 218 ± 64° (1183)	$0.7 \pm 1.4$ 253° (541)
AMIGOS-3c Aqd25 786 m Channel Site (lower) <b>mCDW layer</b> (6976 obs)	$0.2 \pm 1.7$ cm s <sup>-1</sup> 214° (6976 obs)	$0.2 \pm 1.6$ 336° (1411)	$0.3 \pm 2.1$ 178° (1381)	$0.4 \pm 1.5$ 033° (1297)	$0.1 \pm 1.1$ 256° (1191)	$0.1 \pm 1.2$ 96° (1325)	$1.2 \pm 2.1$ 79° (1294)	$0.3 \pm 1.2$ 136° (648)

Units of the entries are shown in the 'All Obs' (all observations) column. Aquadopp unit numbers and depths are from Figure 11. Bold entries indicate periods when flow speed exceeded  $1\sigma$  of the flow speed uncertainty. Total observations exceed the sum of the presented periods because some additional data exists for partial months (months with 400 observations)

## 5. Summary

Ice–ocean interaction has emerged as the primary cause of ice-sheet mass-balance changes in Antarctica, and an important component of glacier evolution in all glacier systems that reach the sea. The areas of this interaction are inherently hard to observe, and yet require long-term monitoring to understand the processes and rates, and to identify causal links with atmospheric and ocean climate. Thus, automated multi-sensor moorings, combining surface, ice and sub-ice sensors will become increasingly important, along with AUVs and instrumented animals, as oceanographic and glaciological research pushes toward a better understanding of the rapid ongoing changes beneath coastal ice. In concert with remote sensing methods, they are key to improved process modeling and ice mass-balance forecasts.

The two AMIGOS-3 stations have provided a host of climate, ice and oceanographic data that document the TEIS in situ conditions over all seasons and for multiple years. The systems illuminate a variety of hard-to-observe processes such as ocean layer properties and flow speed (Dotto and others, 2022); basal ice melting (Wild and others, 2024, in press); winter climate conditions (this study); annual snowfall and high accumulation events (MacLennan and Lenaerts, 2021); and ice flow speed changes, tide height and barometric effects on elevation as the TEIS approaches break-up (this study and Wild and others, 2022). They extend field observational data to year-round, thereby tracking events or activities that occur only at times when logistical access is very difficult. They can also act as in situ weather and surface roughness monitors for aircraft or ground logistical planning.

Future advancements for the AMIGOS multi-sensor systems could include direct integration with Advanced phase-sensitive Radio Echo Sounder (ApRES) installations, which are able to measure basal melt rates and internal strain within the ice column (Lok and others, 2015; Nicholls and others, 2015). Integrating these with the snow height, GPS, ocean sensor and DTS instruments on the AMIGOS-3 would provide a complete local mass-balance suite of measurements. Passive seismic monitoring or acoustic monitoring of the sub-ice water cavity would support studies of basal melting, rifting and calving (e.g. Bartholomaeus and others, 2015; Pettit and others, 2015). Adding an array of GPS receivers that

communicate back to a central AMIGOS using a radio system, or directly back to an internet node, would support ice deformation studies of the region surrounding the station.

The addition of the DTS systems in the AMIGOS-3 has led to a significant improvement in the ability to track temperature and thickness variations of sub-ice ocean cavity water types, as well as the basal freeze-on or melting rates at the ice–ocean interface. This addition, with its attendant need for power management due to the high power requirements, was made possible by the two-way communication afforded by the Iridium data link. However, integrating the DTS, and the potential additions of ApRES and acoustic or video monitors, points to the need for much greater data rates for uplinking. Incorporating either Iridium NEXT or Starlink into a future AMIGOS system would greatly enhance this control and station monitoring capability, and would support much greater data transfer rates.

A persistent issue with all automated data station installations on the ice sheets or ice shelves (at least those in accumulating regions) is burial by snow. Revisiting remote automated stations is logistically difficult, and the increasing number of these stations makes timely revisits hard to achieve. An engineering design that incorporates automated periodic raising of the station should be a goal for future polar or glacier surface instrument stations.

**Supplementary material.** The supplementary material for this article can be found at <https://doi.org/10.1017/jog.2024.96>.

**Data availability statement.** The AMIGOS-3 data are available from the United States Antarctic Program Data Center (USAP-DC), at <https://www.usap-dc.org/view/project/p0010162>. Hugin data are available from the Swedish National Data service: <https://snd.gu.se/en/catalogue/dataset/2020-193-1/1>. A summary of the various sensor acquisitions is given in Figure S4.

**Acknowledgements.** The authors would like to thank the many field support and logistics people at Antarctic Support Contractors, and our colleagues in the International Thwaites Glacier Collaboration (ITGC) Thwaites-Amundsen Regional Survey and Network (TARSAN) project in December–January 2019–2020, 2021–2022, and 2022–2023. We also thank the KOPRI logistics and field team (D. Pomraning, J-S Kim) for the Nansen Ice Shelf AMIGOS-3 prototype installation in January–February of 2017. Additional support was provided

by the Centers for Transformative Environmental Monitoring Programs under NSF EAR-1832109.

**Author contributions.** TAS and RR conceived of the AMIGOS design and sensor array; TW assembled and tested the AMIGOS-3 units; BW wrote the final operating code; SA, SE, RE, CM, JS, ET, and RW provided the initial sensor integration with the operating system; MT, EP, KA, and AM assisted in the field installation and data set descriptions; TD and AW contributed to the oceanographic discussion; TAS led the writing; and all co-authors provided comments and edits.

**Funding statement.** This work is part of the Thwaites-Amundsen Regional Survey and Network (TARSAN) project within the NSF-OPP—NERC International Thwaites Glacier Collaboration program ([www.thwaitesglacier.org](http://www.thwaitesglacier.org)). Funding for aspects of the AMIGOS-2 and -3 development came from an NSF EAGER Grant OPP-1441432, and from the TARSAN award, OPP-1738992. The student sensor integration team was funded under the University of Colorado Boulder Space Grant program. ITGC contribution number 093.

**Competing interests.** The authors declare no competing interests.

## References

- Alley KE and 10 others (2021) Two decades of dynamic change and progressive destabilization on the Thwaites Eastern Ice Shelf. *The Cryosphere* 15(11), 5187–5203. doi: [10.5194/tc-15-5187-2021](https://doi.org/10.5194/tc-15-5187-2021)
- Arzeno IB and 7 others (2014) Ocean variability contributing to basal melt rate near the ice front of Ross Ice Shelf, Antarctica. *Journal of Geophysical Research: Oceans* 119(7), 4214–4233. doi: [10.1002/2014JC009792](https://doi.org/10.1002/2014JC009792)
- Bartholomaeus TC, Larsen CF, West ME, O'Neel S, Pettit EC and Truffer M (2015) Tidal and seasonal variations in calving flux observed with passive seismology. *Journal of Geophysical Research: Earth Surface* 120(11), 2318–2337. doi: [10.1002/2015JF003641](https://doi.org/10.1002/2015JF003641)
- Cape MR, Vernet M, Skvarca P, Marinsek S, Scambos TA and Domack E (2015) Foehn winds link climate-driven warming to ice shelf evolution in Antarctica. *Journal of Geophysical Research: Atmospheres* 120, 11037–11057. doi: [10.1002/2015JD023465](https://doi.org/10.1002/2015JD023465)
- Caton Harrison T and 6 others (2022) Reanalysis representation of low-level winds in the Antarctic near-coastal region. *Weather and Climate Dynamics* 3(4), 1415–1437. doi: [10.5194/wcd-3-1415-2022](https://doi.org/10.5194/wcd-3-1415-2022)
- Doble MJ, Wilkinson JP, Valcic L, Robst J, Tait A and Preston M (2017) Robust wavebuoys for the marginal ice zone: experiences from a large array in the Beaufort Sea. *Elementa: Science of the Anthropocene* 5, 47. doi: [10.1525/elementa.233](https://doi.org/10.1525/elementa.233)
- Dotto TS and 10 others (2022) Ocean variability beneath Thwaites Eastern Ice Shelf driven by the Pine Island Bay Gyre strength. *Nature Communications* 13(1), 7480. doi: [10.1038/s41467-022-35499-5](https://doi.org/10.1038/s41467-022-35499-5)
- Gade HG (1979) Melting of ice in sea water: a primitive model with application to the Antarctic ice shelf and icebergs. *Journal of Physical Oceanography* 9(1), 189–198. doi: [10.1175/1520-0485\(1979\)009<0189:MOIISW>2.0.CO;2](https://doi.org/10.1175/1520-0485(1979)009<0189:MOIISW>2.0.CO;2)
- Hattermann T and 8 others (2021) Observed interannual changes beneath Filchner-Ronne Ice Shelf linked to large-scale atmospheric circulation. *Nature Communications* 12(1), 2961. doi: [10.1038/s41467-021-23131-x](https://doi.org/10.1038/s41467-021-23131-x)
- Hattermann T, Nøst OA, Lilly JM and Smedsrud LH (2012) Two years of oceanic observations below the Fimbul Ice Shelf, Antarctica. *Geophysical Research Letters* 39(12), L12605. doi: [10.1029/2012GL051012](https://doi.org/10.1029/2012GL051012)
- Hausner MB, Suárez F, Glander KE, Van de Giesen N, Selker JS and Tyler SW (2011) Calibrating single-ended fiber-optic Raman spectra distributed temperature sensing data. *Sensors* 11(11), 10859–10879. doi: [10.3390/s111110859](https://doi.org/10.3390/s111110859)
- Herráiz-Borreguero L and 6 others (2016) Basal melt, seasonal water mass transformation, ocean current variability, and deep convection processes along the Amery Ice Shelf calving front, East Antarctica. *Journal of Geophysical Research: Oceans* 121(7), 4946–4965. doi: [10.1002/2016JC011858](https://doi.org/10.1002/2016JC011858)
- Howard SL, Erofeeva S and Padman L (2019) CATS2008: Circum-Antarctic Tidal Simulation Version 2008. U.S. Antarctic Program (USAP) Data Center.
- Kobs S, Holland DM, Zagorodnov V, Stern A and Tyler SW (2014) Novel monitoring of Antarctic ice shelf basal melting using a fiber-optic distributed temperature sensing mooring. *Geophysical Research Letters* 41(19), 6779–6786. doi: [10.1002/2014GL061155](https://doi.org/10.1002/2014GL061155)
- Krishfield R, Toole J, Proshutinsky A and Timmermans ML (2008) Automated ice-tethered profilers for seawater observations under pack ice in all seasons. *Journal of Atmospheric and Oceanic Technology* 25(11), 2091–2105. doi: [10.1175/2008JTECH0587.1](https://doi.org/10.1175/2008JTECH0587.1)
- Lee CK and 9 others (2019) Seasonal variability of basal melt under the Nansen Ice Shelf, Antarctica. In AGU Fall Meeting Abstracts (vol. 2019, C21D–1475).
- Lee CM, Thomson J and Marginal and Ice Zone and Arctic Sea State Teams (2017) An autonomous approach to observing the seasonal ice zone in the western Arctic. *Oceanography* 30(2), 56–68. doi: [10.5670/oceanog.2017.222](https://doi.org/10.5670/oceanog.2017.222)
- Lee WS and 6 others (2016) Multi-disciplinary observation network to monitor cryospheric changes in the Northern Victoria Land, Antarctica. In AGU Fall Meeting Abstracts (C13C–0854).
- Lok LB, Brennan PV, Ash M and Nicholls KW (2015) Autonomous phase-sensitive radio echo sounder for monitoring and imaging Antarctic ice shelves. In 8th International Workshop on Advanced Ground Penetrating Radar (IWAGPR) (1–4). IEEE
- MacLennan ML and Lenaerts JT (2021) Large-scale atmospheric drivers of snowfall over Thwaites Glacier, Antarctica. *Geophysical Research Letters* 48(17), e2021GL093644. doi: [10.1029/2021GL093644](https://doi.org/10.1029/2021GL093644)
- MacLennan ML and 9 others (2023) Climatology and surface impacts of atmospheric rivers on West Antarctica. *The Cryosphere* 17(2), 865–881. doi: [10.5194/tc-17-865-2023](https://doi.org/10.5194/tc-17-865-2023)
- Münchow A, Padman L, Washam P and Nicholls KW (2016) The ice shelf of Petermann Gletscher, North Greenland, and its connection to the Arctic and Atlantic Oceans. *Oceanography* 29(4), Special Issue on Ocean-Ice Interaction. <https://www.jstor.org/stable/24862284>. doi: [10.5670/oceanog.2016.101](https://doi.org/10.5670/oceanog.2016.101)
- Nicholls KW (2018) The study of ice shelf-ocean interaction—Techniques and recent results. *Advances in Polar Science* 29(3), 222–230. doi: [10.13679/j.advps.2018.3.00222](https://doi.org/10.13679/j.advps.2018.3.00222)
- Nicholls KW, Corr HF, Stewart CL, Lok LB, Brennan PV and Vaughan DG (2015) A ground-based radar for measuring vertical strain rates and time-varying basal melt rates in ice sheets and shelves. *Journal of Glaciology* 61(230), 1079–1087. doi: [10.3189/2015JG15J073](https://doi.org/10.3189/2015JG15J073)
- Padman L, King M, Goring D, Corr H and Coleman R (2003) Ice-shelf elevation changes due to atmospheric pressure variations. *Journal of Glaciology* 49(167), 521–526. doi: [10.3189/172756503781830386](https://doi.org/10.3189/172756503781830386)
- Pettit EC, Lee KM, Brann JP, Nystuen JA, Wilson PS and O'Neel S (2015) Unusually loud ambient noise in tidewater glacier fjords: a signal of ice melt. *Geophysical Research Letters* 42(7), 2309–2316. doi: [10.1002/2014GL062950](https://doi.org/10.1002/2014GL062950)
- Polashenski C, Perovich D, Richter-Menge J and Elder B (2011) Seasonal ice mass-balance buoys: adapting tools to the changing Arctic. *Annals of Glaciology* 52(57), 18–26. doi: [10.3189/172756411795931516](https://doi.org/10.3189/172756411795931516)
- Scambos TA and 8 others (2013) A camera and multisensor automated station design for polar physical and biological systems monitoring: AMIGOS. *Journal of Glaciology* 59(214), 303–314. doi: [10.3189/2013JG12J170](https://doi.org/10.3189/2013JG12J170)
- Scambos T and 7 others (2009) Ice shelf disintegration by plate bending and hydro-fracture: satellite observations and model results of the 2008 Wilkins ice shelf break-ups. *Earth and Planetary Science Letters* 280(1–4), 51–60. doi: [10.1016/j.epsl.2008.12.027](https://doi.org/10.1016/j.epsl.2008.12.027)
- Scambos T and 7 others (2008) Calving and ice-shelf break-up processes investigated by proxy: Antarctic tabular iceberg evolution during northward drift. *Journal of Glaciology* 54(187), 579–591. doi: [10.3189/002214308786570836](https://doi.org/10.3189/002214308786570836)
- Shaw WJ, Stanton TP, McPhee MG and Kikuchi T (2008) Estimates of surface roughness length in heterogeneous under-ice boundary layers. *Journal of Geophysical Research: Oceans* 113, C08030. doi: [10.1029/2007JC004550](https://doi.org/10.1029/2007JC004550)

- Stanton TP and 8 others** (2013) Channelized ice melting in the ocean boundary layer beneath Pine Island Glacier, Antarctica. *Science* **341**(6151), 1236–1239. doi: [10.1126/science.1239373](https://doi.org/10.1126/science.1239373)
- Tyler SW and 8 others** (2013) Using distributed temperature sensors to monitor an Antarctic ice shelf and sub-ice-shelf cavity. *Journal of Glaciology* **59**(215), 583–591. doi: [10.3189/2013JoG12J207](https://doi.org/10.3189/2013JoG12J207)
- Van Wessem JM and 7 others** (2016) The modelled surface mass balance of the Antarctic Peninsula at 5.5 km horizontal resolution. *The Cryosphere* **10**(1), 271–285. doi: [10.5194/tc-10-271-2016](https://doi.org/10.5194/tc-10-271-2016)
- Wählin AK and 8 others** (2021) Pathways and modification of warm water flowing beneath Thwaites Ice Shelf, West Antarctica. *Science Advances* **7**(15), eabd7254. doi: [10.1126/sciadv.abd7254](https://doi.org/10.1126/sciadv.abd7254)
- Washam P, Nicholls KW, Münchow A and Padman L** (2019) Summer surface melt thins Petermann Gletscher Ice Shelf by enhancing channelized basal melt. *Journal of Glaciology* **65**(252), 662–674. doi: [10.1017/jog.2019.43](https://doi.org/10.1017/jog.2019.43)
- Wellner JS and 10 others** (2019) The Larsen Ice Shelf System, Antarctica (LARISSA): polar systems bound together, changing fast. *GSA Today* **29**(8). doi: [10.1130/GSATG382A.1](https://doi.org/10.1130/GSATG382A.1)
- Wild CT, Alley KE, Muto A, Truffer M, Scambos TA and Pettit EC** (2022) Weakening of the pinning point buttressing Thwaites Glacier, West Antarctica. *The Cryosphere* **16**(2). doi: [10.5194/tc-16-397-2022](https://doi.org/10.5194/tc-16-397-2022)
- Wild CT and 17 others** (2024, in press) Rift propagation signals the last act of the Thwaites Eastern Ice Shelf despite low basal melt rates. *Journal of Glaciology*. doi: [10.1017/jog.2024.64](https://doi.org/10.1017/jog.2024.64)
- Zheng Y, Stevens DP, Heywood KJ, Webber BG and Queste BY** (2022) Reversal of ocean gyres near ice shelves in the Amundsen Sea caused by the interaction of sea ice and wind. *The Cryosphere* **16**(7). doi: [10.5194/tc-16-3005-2022](https://doi.org/10.5194/tc-16-3005-2022)

## Appendix: Hardware and Software Acronyms

ADC	analog to digital converter
ARM	advanced RISC machines
CAN	controller area network
CPU	central processing unit
EMAC	Embedded Microprocessor Manufacturing, a company
FTP	file transfer protocol
GPIO	general-purpose input/output
I <sup>2</sup> C	inter-integrated circuit
I/O	input/output
LIN	local interconnected network
OS	operating system
PCB	printed circuit board
PRT	platinum resistance thermometer
RAM	random access memory
RISC	reduced instruction set computer
RS-232	recommended standard 232 port
SBD	single-burst data
SD/MMC	secure digital/multi-media card
SFTP	secure file transfer protocol
SLC	single-level cell
SODIMM	small outline dual in-line memory module
SSH	secure shell
SPI	serial peripheral interface
USB	universal serial bus